Performance Analysis and Application of Electromagnetic Time Reversal in Source Reconstruction using Finite Difference Time Domain (FDTD) Method

by

Koustubh Bindiganavile Sudarshan

Submitted in partial fulfilment of the requirements
for the degree of Master of Applied Science

at

Dalhousie University
Halifax, Nova Scotia
December 2018

I dedicate this thesis to my Mother and Father for their constant support, motivation and unwavering faith in me

Table of Contents

LIST OF TABLES

LIST OF FIGURES

ABSTRACT

Source reconstruction is a type of an electromagnetic inverse problem that has a wide range of applications. Using the time reversal invariance property of the Maxwell's equations, reconstruction of electromagnetics sources can be realized. In this thesis, the time reversal is achieved using the Finite Difference Time Domain (FDTD) algorithm. The working of such a time reversal operation is demonstrated in a two and a three-dimensions. A part of the thesis is focused on the comparison of the quality of the reconstructed sources with different parameters of the experimental setup. A second method that is used for accurate reconstruction is analyzed with its limitations elaborated. A different method is then presented to fix the limitations of the previous method of time reversal as another part of the thesis. The final part of the thesis simulates a different set-up and checks the validity of using time reversal for a practical application.

ACKNOWLEDGEMENTS

I would like to thank my supervisor Dr. Zhizhang Chen for giving me an opportunity to work on a very fascinating problem. His advice on problem solving and timely guidance made this research very enjoyable.

I am also grateful to my supervisor committee, Dr. Sergey Ponomarenko and Dr. William Phillips for their support and guidance in my research. I would also like to thank Dr. Guy Kember for his insight on complex problems in my research.

My thanks also go to my family and friends; without their constant motivation and engaging discussions, this thesis would not have been possible.

Finally, I would like to thank Nicole Smith and the faculty and the staff of the Electrical engineering department for making my master's degree a smooth journey.

Chapter 1 INTRODUCTION

This thesis aims to extend the research in the area of electromagnetic source reconstruction using time reversal and the finite difference time domain (FDTD) algorithm. Performance analysis of conventional methods for time reversal, analysis of new methods of achieving source reconstruction and a practical application form the core of this thesis.

1.1 BACKGROUND ON FDTD & TIME REVERSAL

The finite difference time domain or FDTD method is an iterative numerical method for solving partial differential equations (PDE). Analytical solutions of partial differential equations are not always feasible due to the constraints placed on the parameters such as geometry and boundaries. Numerical solutions in such situations are the best alternative for obtaining accurate solutions. FDTD is one such numerical method that is exploited for obtaining solutions of PDE's such as Maxwell's equations.

FDTD uses central differencing schemes to approximate partial differentials to obtain their solutions. The FDTD algorithm can be applied using the special time and space staggering lattice introduced by K.S. Yee in 1966 [1]. This method was researched extensively after the introduction of the Yee grid over the years [2, 3, 4, 5]. FDTD is now used for a wide range of applications [6, 7, 8]. One of the applications of FDTD is in computational time reversal of electromagnetic waves. Time reversal is performed by recording the variations of fields in a solution domain, reversing them in time and reinjecting them back into the domain.

Time reversal was applied as an inverse source problem in acoustics [9]. The concept of time reversal was then extended to electromagnetic waves and applied in Telecommunication [10, 11]. Computational Time Reversal of electromagnetic waves was achieved with the help of the Transmission line Matrix (TLM) method [12, 13, 14] and later on with the FDTD algorithm [15, 16].

The time reversal performed for electromagnetic waves is a two-fold process. The electric or magnetic fields generated by a few sources are first recorded at pre-selected points. The field recorded at these points are reversed in time and then reinjected back into the computational domain. This leads to the spatial and temporal focusing at the original source locations generating the fields. A method for source reconstruction using time reversal based on regularised least squares [17, 18] was used to overcome the limitations of conventional time reversal and accurately recover the location and magnitude of the sources generating the fields.

1.2 THESIS OBJECTIVES AND CONTENTS

This thesis demonstrates the conventional time reversal in a two-dimensional cavity surrounded by PEC walls. The performance of such a configuration is analysed with respect to various parameters. The limitations of the conventional time reversal are illustrated.

The method of time reversal based on [17] is verified and applied to new source configurations. The accuracy of the reconstruction of the said configurations is analysed and its limitations are detailed with fail cases. New methods are then presented to fix the limitations and inferences are made.

The use of time reversal in antenna array failure diagnosis in two and three dimensions is analysed as a practical application.

1.3 THESIS ORGANIZATION

Chapter 2 describes the finite difference time domain method that is used extensively in the thesis. It introduces FDTD as a central differencing scheme and explains the limitations with respect to numerical stability and numerical dispersion. The field update equations which are computed iteratively are then derived for the two and the three-dimensional cases.

Chapter 3 describes the theory of time reversal as an electromagnetic inverse problem. The reasoning behind the source localisation after the time reversal operation is also detailed.

Chapter 4 demonstrates the time reversal in two and three dimensions. Parameters to characterise time reversal are discussed, and performance analysis is done by comparing the parameters to different changes in the algorithm.

Chapter 5 explores the limitations of conventional time reversal. A method based on regularised least squares [17] is outlined, and its limitations are elaborated. A potential fix and future work are described after some of the limitations are overcome.

Chapter 6 focuses on the antenna array failure diagnosis application of time reversal in two and three dimensions for both planar and non-planar arrays.

Chapter 7 aims to conclude the results of the thesis and provide the future work and the extensions to the research.

Chapter 2 FINITE DIFFERENCE TIME DOMAIN (FDTD) METHOD

This chapter outlines the procedure used to derive the update equations used for the finite difference time domain algorithm in two and three dimensions.

2.1 CENTRAL DIFFERENCING SCHEME

Consider the Maxwell's equations in one dimension and free space [4]

$$\frac{\partial E_x}{\partial t} = \frac{-1}{\varepsilon_0}\frac{\partial H_y}{\partial z} \ldots\ldots\ldots\ldots (1)$$

$$\frac{\partial H_y}{\partial t} = \frac{-1}{\mu_0}\frac{\partial E_x}{\partial z} \ldots\ldots\ldots\ldots (2)$$

The above equations can be converted to algebraic equations with the help of the central difference scheme. This is obtained with the help of the Taylor series expansion. Each partial differential in the above equation is replaced by its central difference approximations [4].

$$\frac{E_x^{n+1}(m) - E_x^n(m)}{\Delta t} = \frac{-1}{\varepsilon_0}\left(\frac{H_y^{n+\frac{1}{2}}(m+1/2), -H_y^{n+\frac{1}{2}}(m-1/2)}{\Delta z}\right) \ldots\ldots (3)$$

$$\frac{H_y^{n+\frac{1}{2}}(m+1/2) - H_y^{n-\frac{1}{2}}(m+1/2)}{\Delta t} = \frac{-1}{\mu_0}\left(\frac{E_x^n(m+1) - E_x^n(m)}{\Delta z}\right) \ldots\ldots (4)$$

Here $E_x^n(m) = E_x(t = n\Delta t, z = m\Delta z)$, $H_y^{n+\frac{1}{2}}(m+\frac{1}{2}) = H_y(t = (n+\frac{1}{2})\Delta t, z = (m+\frac{1}{2})\Delta z)$,

$\Delta t$is the discretizing time step and Δz is the spatial step, n represents the time steps index with half increments, m represents the space steps index also with half increments in accordance with the staggered space and time steps suggested by [1]. The above equation from the so-called the leap-frog algorithm due to its peculiar time and space stepping

iterative computation. The following sections derive the update equations used in the two and the three dimensions of the FDTD algorithm.

2.2 TWO-DIMENSIONAL LATTICE ARRANGEMENT

The update equations that are going to be derived are done so in the context of the software package MATLAB. The software does not permit any half time or space step. Hence, the update equations are derived in an alternate manner while adhering to the rules of the Yee Algorithm. A small computational grid with 8 grid points in the x-direction (horizontal) and 6 grid points in the y-direction (vertical) is chosen as the reference for the derivation.

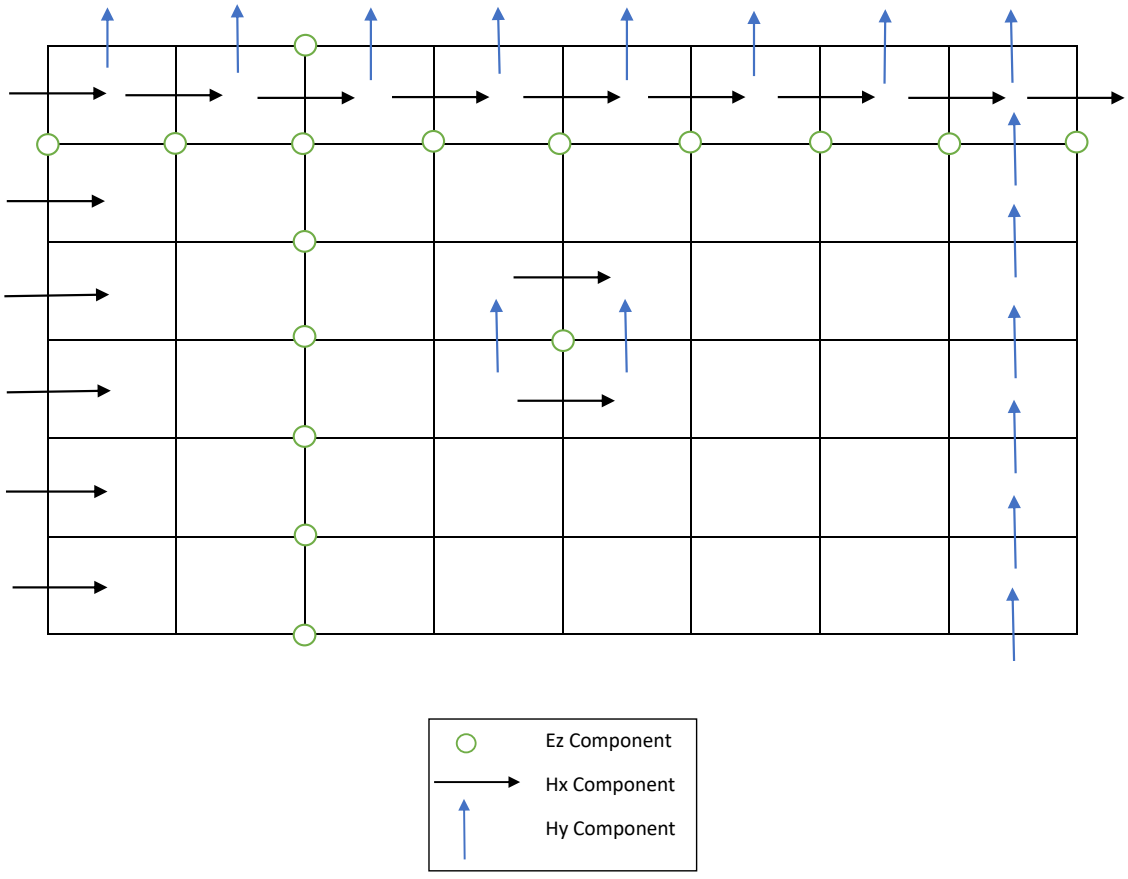

Figure 2.1 Computational grid reference used for the derivation of the update equations of the FDTD algorithm and the legend of the symbols used for different field components

The TM mode of propagation is selected for the update equations containing E_z, H_x and H_y as the field components. Figure 2.1 describes the two-dimensional lattice arrangement used for the FDTD simulation in MATLAB. The horizontal right arrows coloured in black represent the H_x component, the vertical arrows coloured in blue represent the H_y component and the circles coloured in red placed in the intersections of the grid represent the E_z component. The two types of arrows are placed at a distance of half the size of the single cell in the lattice to conform to the arrangement proposed in [1]. The unit cell length in the x-direction is Δx and in the y-direction is Δy. The distance between two of the same field components as H_x and H_x in the grid is Δx or Δy depending on the direction. The distance between any two different field components like H_x and E_z is $\Delta x/2$ or $\Delta y/2$ depending on the direction. In addition, E_z component is surrounded by H_x and H_y components, forming the Yee's grid.

As shown in Fig. 2.2, the example gives an 8 x 6 matrix for the Ez component, 8 x 7 matrix for the Hx component and a 7 x 6 matrix for the Hy Matrix for the chosen lattice as seen in Figure 2.2. In general, if Nx is the total number of grid points in the x-direction and Ny if that in the y-direction, the Ez component needs a Nx x Ny matrix, the Hx component needs a Nx x (Ny-1) matrix and the Hy needs a (Nx-1) x Ny matrix. Similar matrix allocations can be used for TE mode of propagation as well as the three-dimensional equations. These matrices are iteratively updated using the update equations that are going to be derived in section 2.3 for a total simulation time chosen according to the requirements of the simulation.

2.3 THE TWO DIMENSIONAL FDTD UDATE EQUATIONS

[4] details the derivation of the update equations for FDTD. Maxwell's equations in two dimensions are [4]:

$$\frac{\partial H_x}{\partial t} = \frac{1}{\mu}\left[\frac{-\partial E_z}{\partial y} - \sigma_x H_x\right] \dots\dots (5)$$

$$\frac{\partial H_y}{\partial t} = \frac{1}{\mu}\left[\frac{\partial E_z}{\partial x} - \sigma_y H_y\right] \dots\dots (6)$$

$$\frac{\partial E_z}{\partial t} = \frac{1}{\varepsilon}\left[\frac{\partial H_y}{\partial x} - \frac{\partial H_x}{\partial y} - \sigma_z E_z\right] \ldots\ldots (7)$$

where ε is the permittivity of the medium and μ is the permeability of the medium. Most of the simulations in this thesis uses free space. Hence the free-space permittivity ε_0 and the free space permeability μ_0 are used in the following FDTD derivations. The electric and magnetic conductivities that are present in the Maxwell's equations are ignored as they are not in the scope of this thesis study.

The FDTD approximations for the above equations are then applied and the following FDTD equations are obtained [4]:

$$H_x^{n+1/2} = H_x^{n-\frac{1}{2}}(i,j) + \frac{-\Delta t}{\mu_0 \mu_x(i,j)\Delta y}[E_z^n(i,j+1) - E_z^n(i,j)] \ldots\ldots (8)$$

$$H_y^{n+1/2} = H_y^{n-\frac{1}{2}}(i,j) + \frac{-\Delta t}{\mu_0 \mu_x(i,j)\Delta x}[E_z^n(i+1,j) - E_z^n(i,j)] \ldots\ldots (9)$$

$$E_z^{n+1}(i,j) = E_z^n(i,j) + \frac{\Delta t}{\varepsilon_0 \varepsilon_z(i,j)}\left[\frac{H_y^{n+\frac{1}{2}}(i,j) - H_y^{n+\frac{1}{2}}(i-1,j)}{\Delta x} - \frac{H_x^{n+\frac{1}{2}}(i,j) - H_x^{n+\frac{1}{2}}(i,j-1)}{\Delta y}\right] \ldots\ldots (10)$$

Here $E_z^n(i,j) = E_z(t = n\Delta t, x = i\Delta x, y = j\Delta y)$,

$H_x^{n+\frac{1}{2}}(i,j) = H_x(t = (n+\frac{1}{2})\Delta t, x = i\Delta x, y = (j+\frac{1}{2})\Delta y)$,

$H_y^{n+\frac{1}{2}}(i,j) = H_y(t = (n+\frac{1}{2})\Delta t, x = (i+\frac{1}{2})\Delta x, y = j\Delta y)$

i and j represent the indices of the spatial steps, n represents the index of the time step. The three update equations are repeated for the total number of iterations with source. Δx is the space step in the x-direction, Δy is the space step in the y-direction and Δt is the temporal step.

The space steps Δx and Δy are chosen with the help of the maximum frequency used in the simulation. $\Delta x \; or \; \Delta y$ is calculated as follows [4]

$$lam_0 = \frac{f_{max}}{C_0} \dots\dots (11)$$

$$\max(\Delta x, \Delta y) = \frac{lam_0}{NRES * Nmax} \dots\dots (12)$$

In the above calculations, lam_0 is the shortest wavelength concerned. $NRES$ is the resolution factor for the shortest wavelength, C_0 is the speed of light and $Nmax$ is the maximum refractive index of the medium which is equal to unity in most of the simulations in this thesis. The value of $NRES$ can range from 10, 20, 50 to 100 depending on the use of finer or coarser grids for different applications.

The choices of the three grid parameters, i.e. $\Delta x, \Delta y, \Delta t$, also need to satisfy the stability condition [19]. For two-dimensional FDTD, the stability condition is [4]

$$\Delta t < \frac{1}{C_0 \sqrt{\left(\frac{1}{\Delta x}\right)^2 + \left(\frac{1}{\Delta y}\right)^2}} \dots\dots (13)$$

Another factor that must be considered while developing the FDTD algorithm is the effects of numerical dispersion. Numerical dispersion is the phase difference that arises between the physical and the FDTD modelled EM wave. The propagation velocity of the EM wave V_p can be written in terms of its angular velocity ω and the wave number κ as [4]

$$V_p = \frac{\omega}{\kappa}$$

Numerical dispersion relations for the physical EM wave as well as the FDTD modelled EM wave are established for the comparison of the propagation velocities of the two waves

[4]. They measure the errors as the result of FDTD discretization of a continuous space for Maxwell's equations. The numerical dispersion relations that are used for the analysis of the propagation velocity of the EM wave in the physical and the numerical domain in two-dimensions are given respectively by [4]

$$\frac{\omega^2}{{C_0}^2} = \kappa_x^2 + \kappa_y^2 \ldots\ldots (14)$$

$$\left[\frac{1}{C_0 \Delta t} sin\left(\frac{\omega \Delta t}{2}\right)\right]^2 = \left[\frac{1}{\Delta x} sin\left(\frac{\kappa_x \Delta x}{2}\right)\right]^2 + \left[\frac{1}{\Delta y} sin\left(\frac{\kappa_y \Delta y}{2}\right)\right]^2 \ldots\ldots (15)$$

Comparing the above two dispersion relations, the numerical velocity of propagation is lower than the physical velocity of propagation of propagation which is equal to the speed of light causing dispersion errors in numerical solutions. The numerical velocity is made to approach the value of the physical velocity which is equal to the speed of light by making time and space steps small enough [4].

2.4 THE THREE-DIMENSIONAL FDTD UPDATE EQUATIONS

The update equations for the three-dimensional FDTD is derived [4] in the same manner as that as Section 2.2. The Maxwell's Equation in 3 dimensions in free space are [4]

$$\frac{\partial H_x}{\partial t} = \frac{1}{\mu_0}\left[\frac{\partial E_y}{\partial z} - \frac{\partial E_z}{\partial y}\right] \ldots\ldots (17)$$

$$\frac{\partial H_y}{\partial t} = \frac{1}{\mu_0}\left[\frac{\partial E_z}{\partial x} - \frac{\partial E_x}{\partial z}\right] \ldots\ldots (18)$$

$$\frac{\partial H_z}{\partial t} = \frac{1}{\mu_0}\left[\frac{\partial E_x}{\partial y} - \frac{\partial E_y}{\partial x}\right] \ldots\ldots (19)$$

$$\frac{\partial E_x}{\partial t} = \frac{1}{\varepsilon_0}\left[\frac{\partial H_z}{\partial y} - \frac{\partial H_y}{\partial z}\right] \ldots\ldots (20)$$

$$\frac{\partial E_y}{\partial t} = \frac{1}{\varepsilon_0}\left[\frac{\partial H_x}{\partial z} - \frac{\partial H_z}{\partial x}\right] \ldots\ldots (21)$$

$$\frac{\partial E_z}{\partial t} = \frac{1}{\varepsilon_0}\left[\frac{\partial H_y}{\partial x} - \frac{\partial H_x}{\partial y}\right] \ldots\ldots (22)$$

By replacing the partial differentials in the above equations with their FDTD approximations, the final update equations are [4]

$$H_x^{n+\frac{1}{2}}(i,j,k) = \left[\frac{1-\frac{\Delta t}{2\mu}}{1+\frac{\Delta t}{2\mu}}\right] H_x^{n-\frac{1}{2}}(i,j,k) + \left[\frac{\Delta t}{\mu\left(1+\frac{\Delta t}{2\mu}\right)}\right]\left[\frac{E_y^n(i,j,k+1)-E_y^n(i,j,k)}{\Delta z}\right] - \left[\frac{E_z^n(i,j+1,k)-E_z^n(i,j,k)}{\Delta y}\right] \dots\dots (23)$$

$$H_y^{n+\frac{1}{2}}(i,j,k) = \left[\frac{1-\frac{\Delta t}{2\mu}}{1+\frac{\Delta t}{2\mu}}\right] H_y^{n-\frac{1}{2}}(i,j,k) + \left[\frac{\Delta t}{\mu\left(1+\frac{\Delta t}{2\mu}\right)}\right]\left[\frac{E_z^n(i+1,j,k)-E_z^n(i,j,k)}{\Delta x}\right] - \left[\frac{E_x^n(i,j,k+1)-E_x^n(i,j,k)}{\Delta z}\right] \dots\dots (24)$$

$$H_z^{n+\frac{1}{2}}(i,j,k) = \left[\frac{1-\frac{\Delta t}{2\mu}}{1+\frac{\Delta t}{2\mu}}\right] H_z^{n-\frac{1}{2}}(i,j,k) + \left[\frac{\Delta t}{\mu\left(1+\frac{\Delta t}{2\mu}\right)}\right]\left[\frac{E_x^n(i,j+1,k)-E_x^n(i,j,k)}{\Delta y}\right] - \left[\frac{E_y^n(i+1,j,k)-E_y^n(i,j,k)}{\Delta x}\right] \dots\dots (25)$$

$$E_x^{n+1}(i,j,k) = \left[\frac{1-\frac{\Delta t}{2\varepsilon}}{1+\frac{\Delta t}{2\varepsilon}}\right] E_x^n(i,j,k) + \left[\frac{\Delta t}{\varepsilon\left(1+\frac{\Delta t}{2\varepsilon}\right)}\right]\left[\frac{H_z^{n+\frac{1}{2}}(i,j,k)-H_z^{n+\frac{1}{2}}(i,j-1,k)}{\Delta y}\right] - \left[\frac{H_y^{n+\frac{1}{2}}(i,j,k)-H_y^{n+\frac{1}{2}}(i,j,k-1)}{\Delta z}\right] \dots\dots (26)$$

$$E_y^{n+1}(i,j,k) = \left[\frac{1-\frac{\Delta t}{2\varepsilon}}{1+\frac{\Delta t}{2\varepsilon}}\right] E_y^n(i,j,k) + \left[\frac{\Delta t}{\varepsilon\left(1+\frac{\Delta t}{2\varepsilon}\right)}\right]\left[\frac{H_x^{n+\frac{1}{2}}(i,j,k) - H_x^{n+\frac{1}{2}}(i,j,k-1)}{\Delta z}\right] - \left[\frac{H_z^{n+\frac{1}{2}}(i,j,k) - H_z^{n+\frac{1}{2}}(i-1,j,k)}{\Delta x}\right] \dots\dots (27)$$

$$E_z^{n+1}(i,j,k) = \left[\frac{1-\frac{\Delta t}{2\varepsilon}}{1+\frac{\Delta t}{2\varepsilon}}\right] E_z^n(i,j,k) + \left[\frac{\Delta t}{\varepsilon\left(1+\frac{\Delta t}{2\varepsilon}\right)}\right]\left[\frac{H_y^{n+\frac{1}{2}}(i,j,k) - H_y^{n+\frac{1}{2}}(i-1,j,k)}{\Delta x}\right] - \left[\frac{H_x^{n+\frac{1}{2}}(i,j,k) - H_x^{n+\frac{1}{2}}(i,j-1,k)}{\Delta y}\right] \dots\dots (28)$$

Here $E_x^n(i,j,k) = E_x(t = n\Delta t, x = (i+\frac{1}{2})\Delta x, y = j\Delta y, z = k\Delta z)$

$$E_y^n(i,j,k) = E_y(t = n\Delta t, x = i\Delta x, y = (j+\tfrac{1}{2})\Delta y, z = k\Delta z)$$

$$E_z^n(i,j,k) = E_z(t = n\Delta t, x = i\Delta x, y = j\Delta y, z = (k+\frac{1}{2})\Delta z)$$

, $H_x^{n+\frac{1}{2}}(i,j,k) = H_x(t = (n+\frac{1}{2})\Delta t, x = i\Delta x, y = (j+\frac{1}{2})\Delta y, z = (k+\frac{1}{2})\Delta z)$

$$H_y^{n+\frac{1}{2}}(i,j,k) = H_y(t = (n+\frac{1}{2})\Delta t, x = (i+\frac{1}{2})\Delta x, y = j\Delta y, z = (k+\frac{1}{2})\Delta z)$$

$$H_z^{n+\frac{1}{2}}(i,j,k) = H_z(t = (n+\frac{1}{2})\Delta t, x = (i+\frac{1}{2})\Delta x, y = (j+\frac{1}{2})\Delta y, z = k\Delta z)$$

A similar equation is used for the calculation of the time step to ensure the stability of the three-dimensional FDTD algorithm [4].

$$\Delta t = \frac{\sqrt{\mu\varepsilon}}{\sqrt{\frac{1}{(\Delta x)^2} + \frac{1}{(\Delta y)^2} + \frac{1}{(\Delta z)^2}}} \ldots\ldots (29)$$

Chapter 3 THEORY OF TIME REVERSAL

This chapter is intended to explain the concept of time reversal as an inverse source problem for source reconstruction. Sections 3.1 and 3.2 elaborate on the theory and procedure of time reversal for source reconstruction. Section 3.3 aims to mathematically detail the peaks obtained at the original source locations after time reversal.

3.1 TIME REVERSAL

If $s1(t)$ is a solution to the governing equations of a physical process, the process is time reversal invariant if $s2(t) = s1(-t)$ is also a solution to the governing equations [29]. The governing equations sometimes have to be modified to fit the time reversal invariance condition [29]. With a few changes to its governing equations, Maxwell's equations exhibit the time reversal invariance property [29].

3.2 TIME REVERSAL AS AN INVERSE SOURCE PROBLEM

The inverse source problem aims to find the cause of a certain event in a physical process with the help of the measurements made from the said event at different points. Time reversal as an inverse source problem has been extensively studied for acoustic waves [9] and experiments have been conducted for electromagnetic waves [11]. The following chapters of the thesis explore time reversal as an inverse source problem for the reconstruction of electromagnetic sources in a cavity. This is realised with the help of the FDTD update equations detailed in the previous section. The data that is recorded from the sources propagating in a certain medium is recorded for the time reversal process with the help of FDTD. This data, that can be collected through measurements contains information regarding the propagation of the sources. After the time reversed data is reinjection back into the problem domain, the sources are reconstructed at their original locations due to the time reversal invariance property. Hence source reconstruction using time reversal forms an important type of an inverse source problem.

3.3 TIME REVERSAL – FIELD PEAK IDENTIFICATION

[17,18] give a detailed explanation on the peak formation of time reversal. This section aims to mathematically explain the peak formation at the original sources' locations.

Consider a cavity with *I* input nodes and *J* output probes. Any input at a node can be considered to be a sum of weighted impulses. An input *x* at a time instant '*n*' can be described as [17]

$$x_i[n] = a_i\delta[n] \dots\dots (30)$$

where $\delta[n]$ is the impulse function and a_i is the magnitude of the *i*th source, *i*=1, 2, 3… *I*.

The field value at the *j*th output node is given by [17,18]

$$y_j[n] = \sum_{i=1}^{I} a_i h_{ij}[n] \dots\dots (31)$$

where $h_{ij}[n]$ is the impulse response at the *j*th output node due to the excitation at the *i*th node. Due to the reciprocity of the domain, $h_{ij}[n] = h_{ji}[n]$; that is, the impulse response at the *j*th output node due to the excitation at the *i*th node is the same as the impulse response at the *i*th output node due to the excitation at the *j*th node.

By reversing the field recorded at the *j*th output node in time and reinjecting it back into the domain, the field at the *i*th input node will be [17,18]

$$X_i[n] = \sum_{j=1}^{J} h_{ij}[n] \circledast y_j[N-1-n] \dots\dots (32)$$

$$X_i[n] = \sum_{j=1}^{J} \sum_{m=0}^{n} h_{ij}[m] \sum_{i=1}^{I} a_i h'_{ij}[N-1-n-m] \dots\dots (33)$$

At the final time step, *n*= $N-1$, the output at each source node from the above equation is the sum of auto-correlation of the impulse responses and the cross-correlation of the impulse responses [17,18].

The auto-correlation between the impulse responses is usually larger compared to the cross-correlation component. Hence a peak is observed at the input nodes after time reversal operation.

Chapter 4 TIME REVERSAL USING THE FDTD METHOD

This chapter introduces the working of source reconstruction using time reversal and FDTD. The space and time focusing of time reversal are first demonstrated in two and three dimensions using impulse sources. The characteristics of the focusing [20,21] are then detailed in the following section. The said characteristics are then analyzed for different configurations of the time reversal experiment used in the first section, and the results are summarized.

4.1 VALIDATION OF THE FDTD ALGORITHM

A rectangular cavity with perfect electric conductor boundaries (PEC) is used to model the effects of a rectangular microwave cavity resonator. The FDTD algorithm can be validated by comparing the simulated resonant frequencies with theoretical solutions. The computational grid is excited by an impulse source placed randomly in the grid. The field values at two random points in the computational domain are recorded, and Fourier transformed to obtain the FDTD numerical solutions. Table 4.1 shows the comparison between the theoretical and FDTD computed resonant frequencies; the FDTD-computed results are obtained by identifying the peaks at two different spatial locations. It can be seen that the resonant frequencies obtained with the FDTD simulations are very close to the theoretical values, thereby validating the FDTD model.

Table 4.1 Theoretical and simulated resonant frequencies of five different modes

Resonant Modes	Theoretical Resonant Frequency (GHz)	Simulated Resonant Frequency – Point #1	Relative Error – Point #1 (%)	Simulated Resonant Frequency – Point #2	Relative Error – Point #2 (%)
TM_{11}	1.0577	1.0633	0.56	1.0600	0.2
TM_{12}	1.5233	1.5203	0.3	1.5344	1.1
TM_{21}	1.8092	1.7338	7.5	1.8597	5.05
TM_{22}	2.1154	2.1199	0.5	2.0294	8.6
TM_{33}	3.1731	3.2838	11.07	3.2895	11.64

4.2 SOURCE RECONSTRUCTION USING THE FDTD METHOD

The concept of source reconstruction using time reversal is demonstrated with the help of a two-dimensional rectangular cavity that is terminated by a perfect electric conductor (PEC) boundary to ensure reflections of the waves at the walls of the cavity. Sections 4.2.1 and 4.2.2 illustrate the space and time focusing properties of time reversal in source reconstruction. Source reconstruction is then demonstrated in three-dimensions in Section 4.2.3. The metrics for the characterization of the focusing are introduced in 4.3 and 4.4 contains the performance analysis with the metrics.

4.2.1 Space Focusing

Space focusing is an essential feature of source reconstruction achieved using time reversal. It makes sure that the sources are reconstructed at their original excitation locations [20]. The rectangular cavity with the PEC walls is considered for the demonstration of space focusing, and the TM mode of propagation is chosen for the excitation of the source. The Ez component is excited by three impulse sources together at the first time step as shown in Figure 4.1 (a). The FDTD algorithm calculates the field components namely Ez, Hx and Hy for each iteration for the total iteration of 1000. The propagation of the Ez component is shown in Figure 4.1(b) as the number of iterations increase. The total simulation time is chosen to allow enough propagation of the excited waves for the length of the cavity. The field values for every iteration is recorded in four pre-chosen output points in the computational grid for time reversal signal processing. The values at these output nodes are recorded for the total iteration number. These values are then reversed in time and reinjected back into the cavity for the total iteration number as shown in Figure 4.1 (c) and Figure 4.1 (d). The three impulse sources are reconstructed in their original excitation location at the end of the final time step characterised by the final iteration number of 1000 as shown in Figure 4.1(e). This clearly verifies the space focusing characteristic of time reversal.

Forward Propagation of 3 sources at time step 1

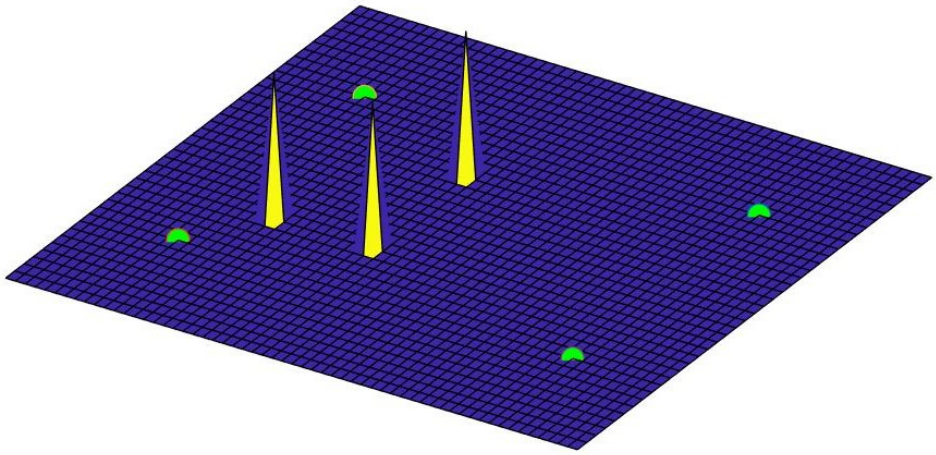

(a)

Forward Propagation of 3 sources at time step 14

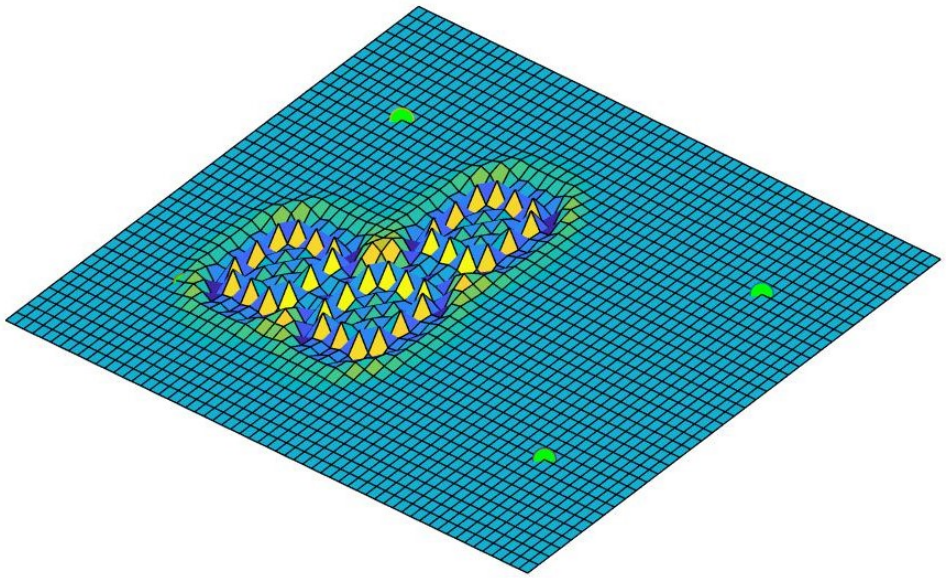

(b)

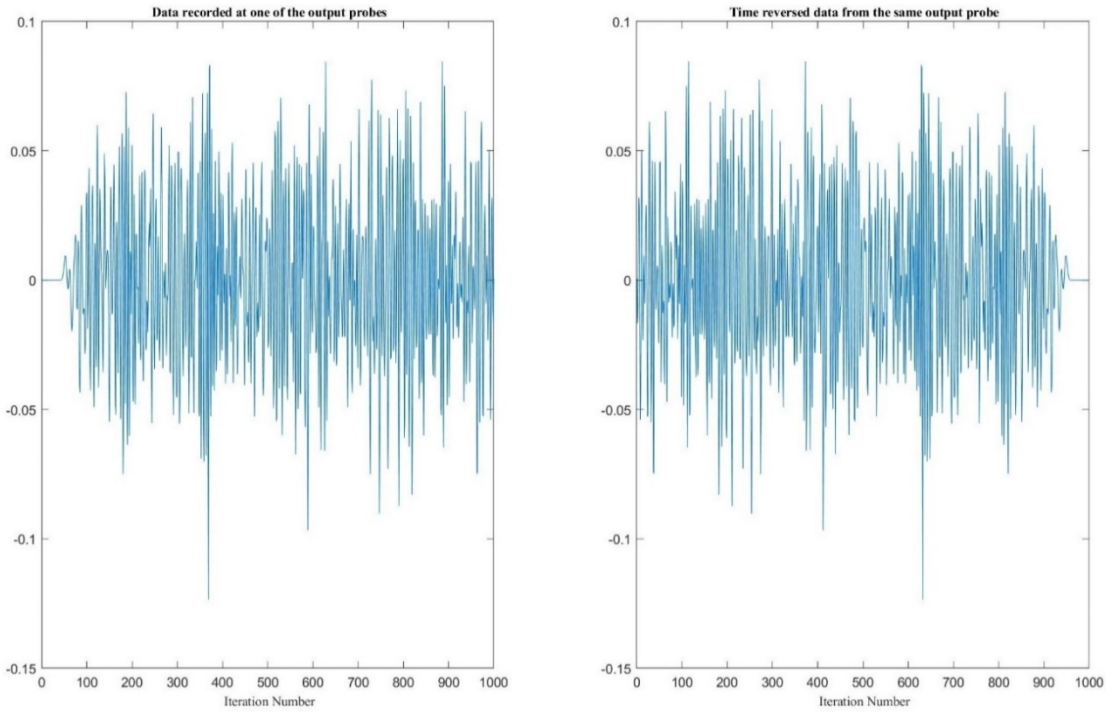

(c)

Reinjection after time reversal at time step 17

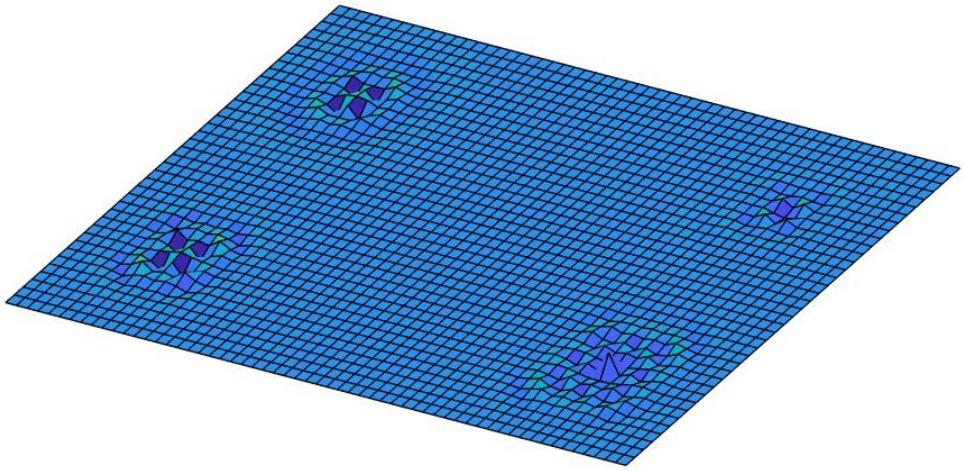

(d)

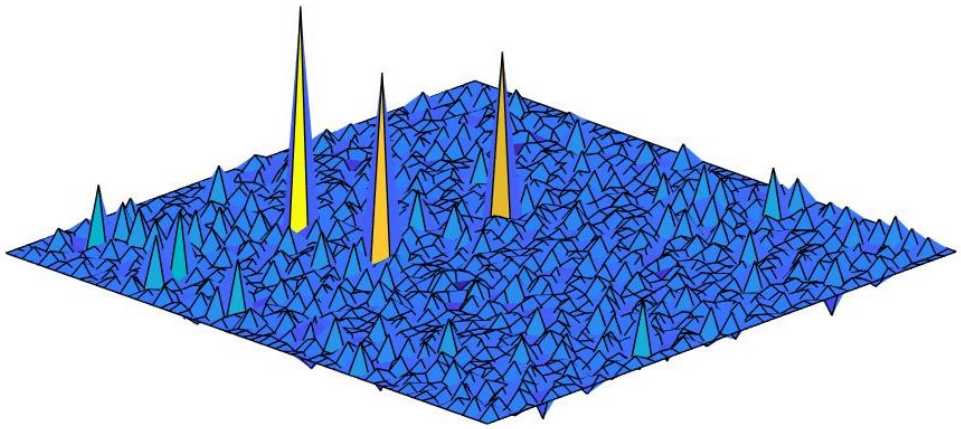

(e)

Figure 4.1 (a) Three impulse sources excited in a 2D PEC cavity with four output probes, (b) FDTD computation of the Ez component , (c) Field values recorded at one output point recorded and reversed in time (d) Reinjection of time reversed fields(e) Final Reconstructed sources localised at their original locations after the total number of iterations(1000).

4.2.2 Time Focusing

The time focusing characteristic of time reversal ensures that the sources are reconstructed at the same time instant that they were excited with the time taken in reverse [20]. The demonstration of space focusing is achieved using the same cavity with PEC walls. But the cavity is now excited by three impulse sources at different time steps. The first impulse source is excited at time step 3, the second at time step 22 and the third at the time step 100 as shown in Figure 4.2 (a) out of the total of 1000 time steps. The field values are recorded at the same four output probes used in Section 4.2.1 and the time reversed data is reinjected back into the cavity. Figure 4.2 (b) shows the time reversed output at the three different time steps mentioned above. The three impulse sources are reconstructed at the same location and at the same time intervals they were initially excited when the total time

interval is considered from the reverse. The first source is reconstructed at the 997th time step, which is the 3rd time step when the time is taken in reverse. Similarly, the second source is reconstructed at the 978th time step and the third at the 900th time step which are the 22nd and 100th time steps in reverse time. This clearly verifies the time compression property of time reversal.

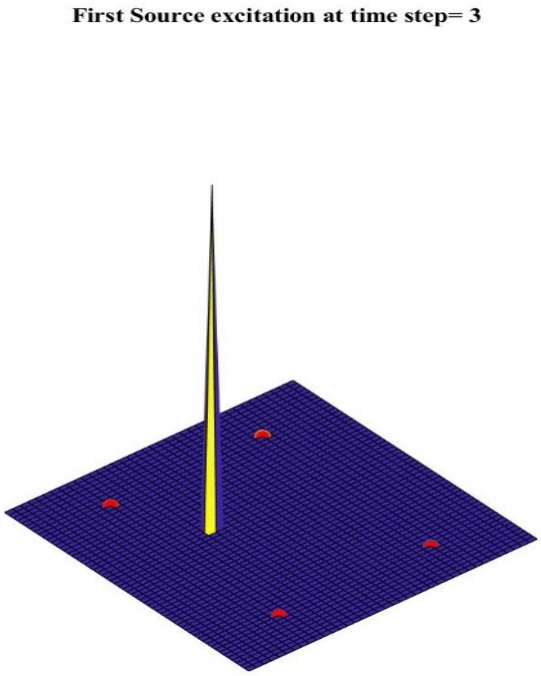

(a)

Second Source excitation at time step= 22

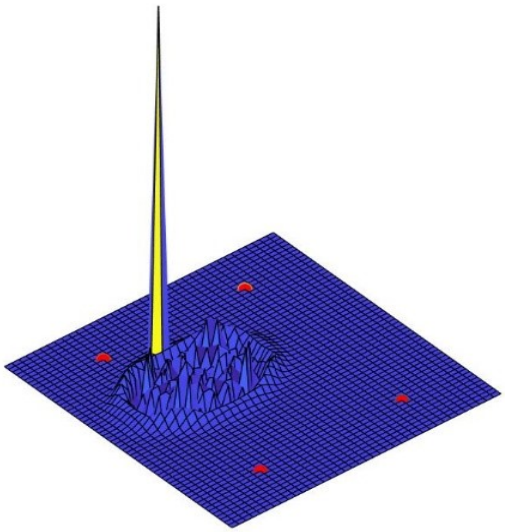

Third Source excitation at time step= 100

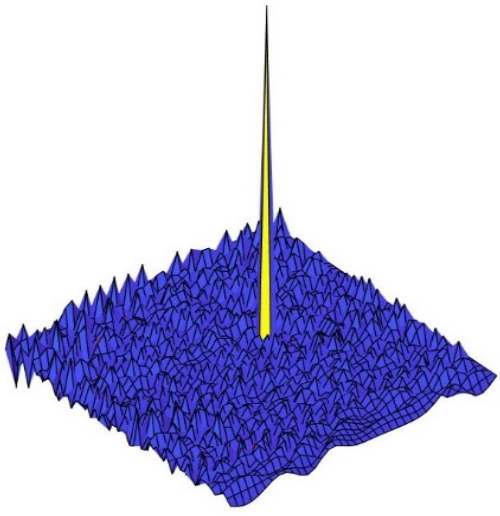

(a)

First Source reconstructed at time step= 997

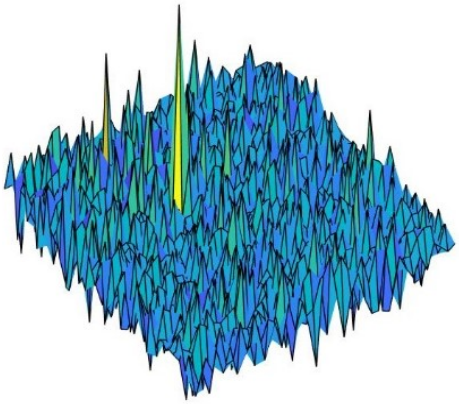

Second Source reconstructed at time step= 978

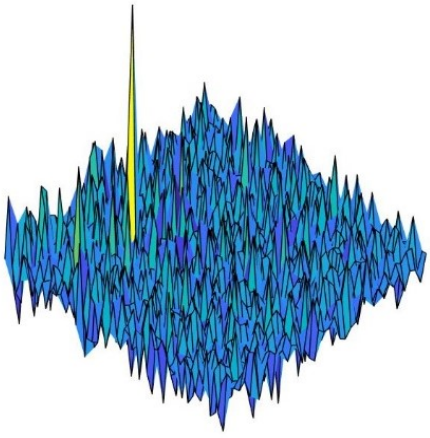

(b)

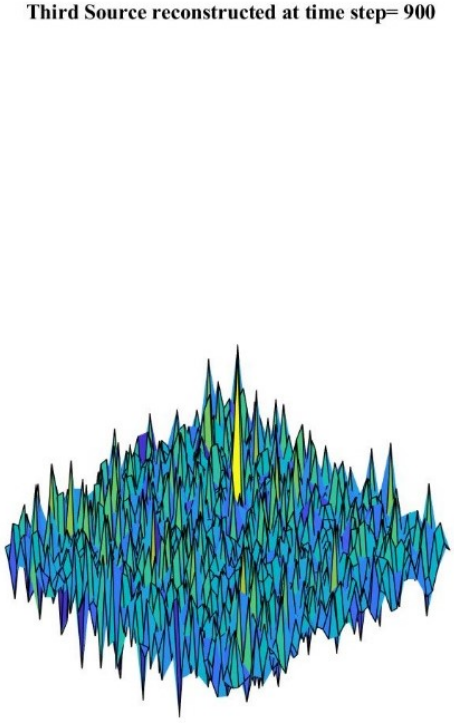

(b)

Figure 4.2 (a) Three impulse sources excited at three different time instances (b) Reconstruction of three sources at the same time instances they were initially excited with time considered in reverse.

4.2.3 Source Reconstruction in three dimensions

To demonstrate the process of time reversal in three-dimensions, a 3D cavity with PEC walls is excited by two impulse sources. 50 FDTD cells are used in all the three directions. The two impulse sources are excited in two different z planes and four output probes are placed in proximity to all the six walls of the cavity as shown in Figure 4.3 (a) and Figure 4.3(b). In figure 4.3(a), the output probes are marked in green circles and the two sources placed in different planes are marked by circles. Figure 4.3(b) shows only the two z-planes in which the sources are located at the first-time step to describe their positions in the 3D cavity. The value of the Ez component is recorded in these output probes and time reversal is performed similar to the two-dimensional case for a total iteration of 3000. The reconstructed sources are shown in Figure 4.3 (c) and 4.3 (d). Similar to the two-

dimensional time reversal, source and time focusing takes place giving peaks at the two source locations.

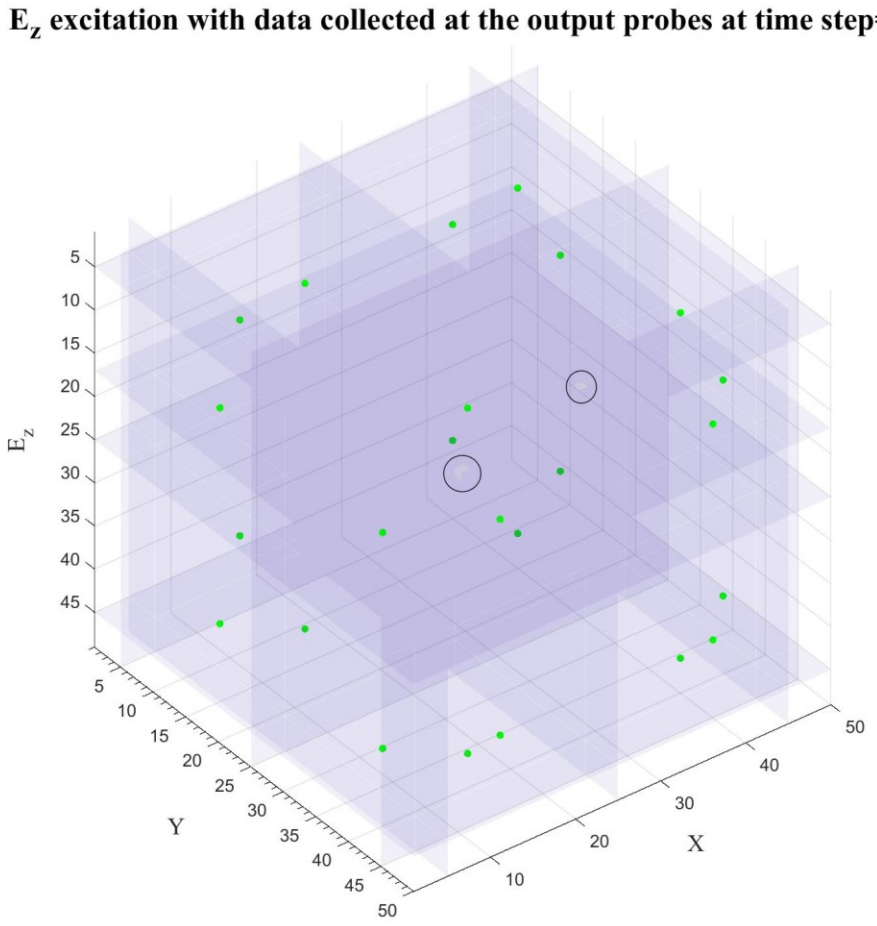

(a)

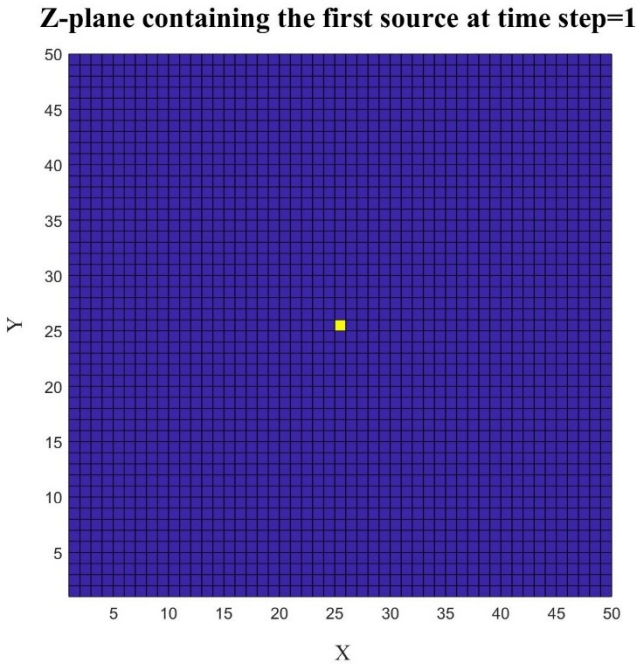
Z-plane containing the first source at time step=1
Y
X
5
10
15
20
25
30
35
40
45
50

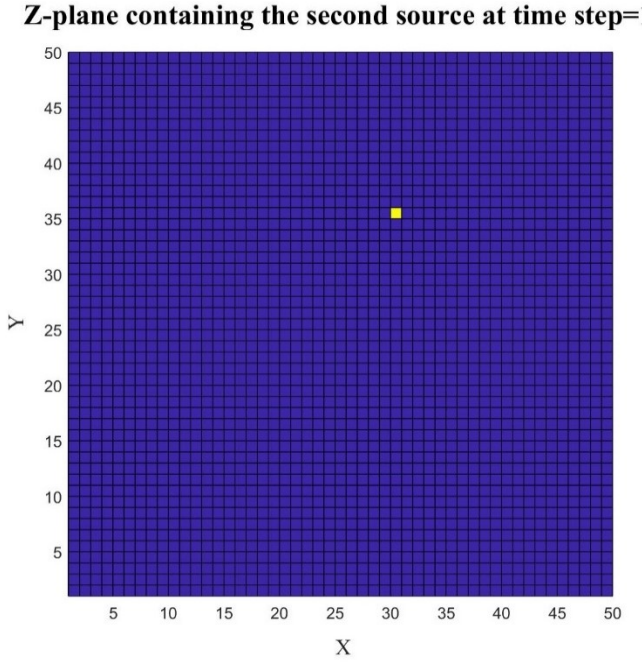
Z-plane containing the second source at time step=1
Y
X
5
10
15
20
25
30
35
40
45
50

(b)

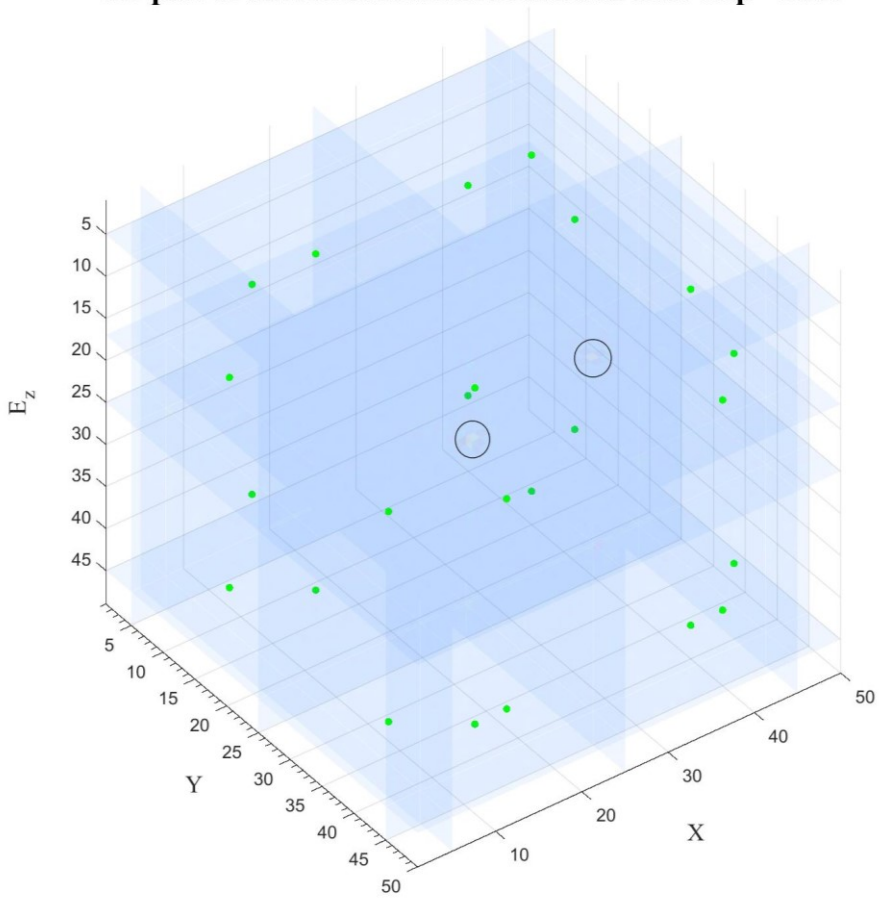
3D plot of the reconstructed sources at time step =3000
E_z
5
10
15
20
25
30
35
40
45
Y
5
10
15
20
25
30
35
40
45
50
X
10
20
30
40
50

(c)

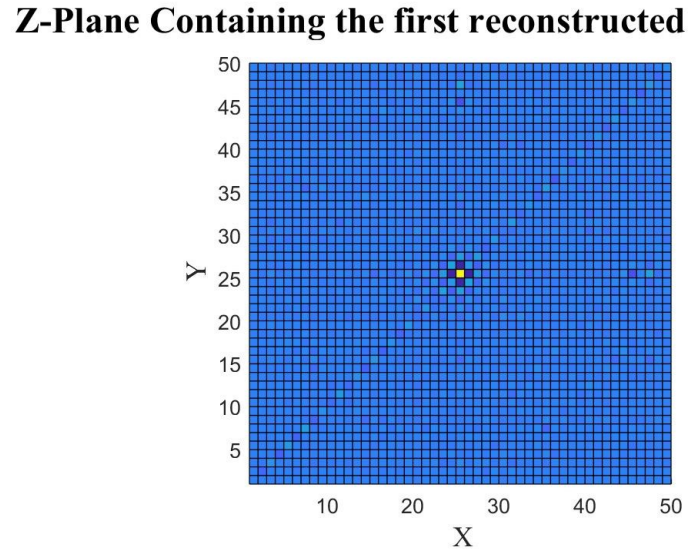

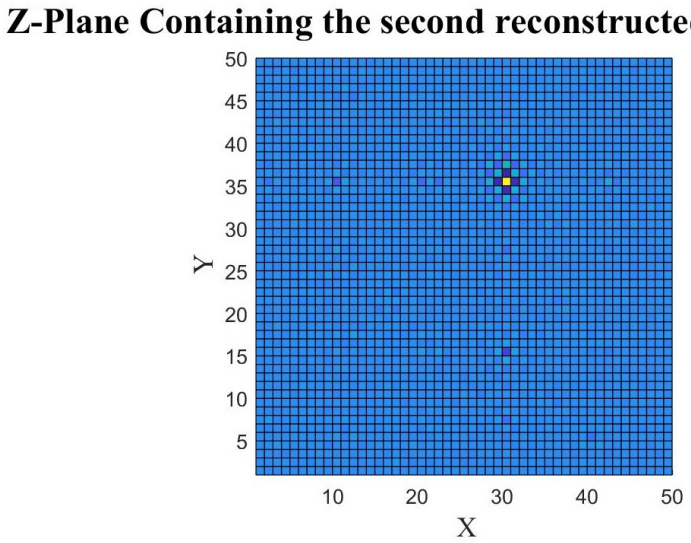

(d)

Figure 4.3 (a) 3D view of the location of the sources and the output probes at time step 1, (b) Z planes containing the 2 sources at time step 1, (c) 3D view of the reconstructed sources. (d) Z-planes of the two reconstructed sources.

4.3 CHARACTERISTICS OF RECONSTRUCTED SOURCES

This section introduces the parameters that are going to be used for the performance analysis of time reversal. Different parameters have been discussed to characterise the spatial and the time focusing of the time-reversed fields in media rich in inducing multipaths [20]. These parameters have been used to analyse the performance of time reversal in a reverberation chamber due to its reflections at the walls [21]. The cavity with the PEC walls that we have used in the previous sections also induces multipaths due to its reflections at the walls and behaves similarly to a reverberation chamber. Hence, these parameters are going to be used to analyse the performance of time reversal of the cavity discussed so far.

4.3.1 Maximum Energy

The first parameter that has been discussed in afore-mentioned literature is the maximum energy of a signal. The maximum energy of a signal $E_z(t, R)$ at time t located at a point R is given by [21]

$$\mathrm{Max(R)} = \max_{t \epsilon N}(|E_z(t, R)\,|^2) \ldots\ldots (34)$$

Here, N is the total duration of the signal E_z and in the simulations that follow this is the total number of iterations of the FDTD algorithm. The maximum energy gives the value of the energy of the reconstructed peak if the objective signal in the above equation is considered at its original source location. This is very useful in finding the value of the reconstructed peak when sources in question are excited at different time intervals. To illustrate the use of Maximum energy, a setup similar to that presented in Section 4.2.2 is considered but with two impulse sources excited at the 50^{th} and the 150^{th} time interval respectively. After the reinjection of the time-reversed fields is done, the square of the absolute value of the position of two sources is plotted for all the time intervals represented by the iteration as shown in Figure 4.4. Each plot clearly shows a peak that is significantly higher than the other values indicating the maximum energy of the reconstructed sources at their original positions. The maximum energy is very representative of the strength of

the reconstructed sources and will be used as a metric for the performance analysis in the following sections.

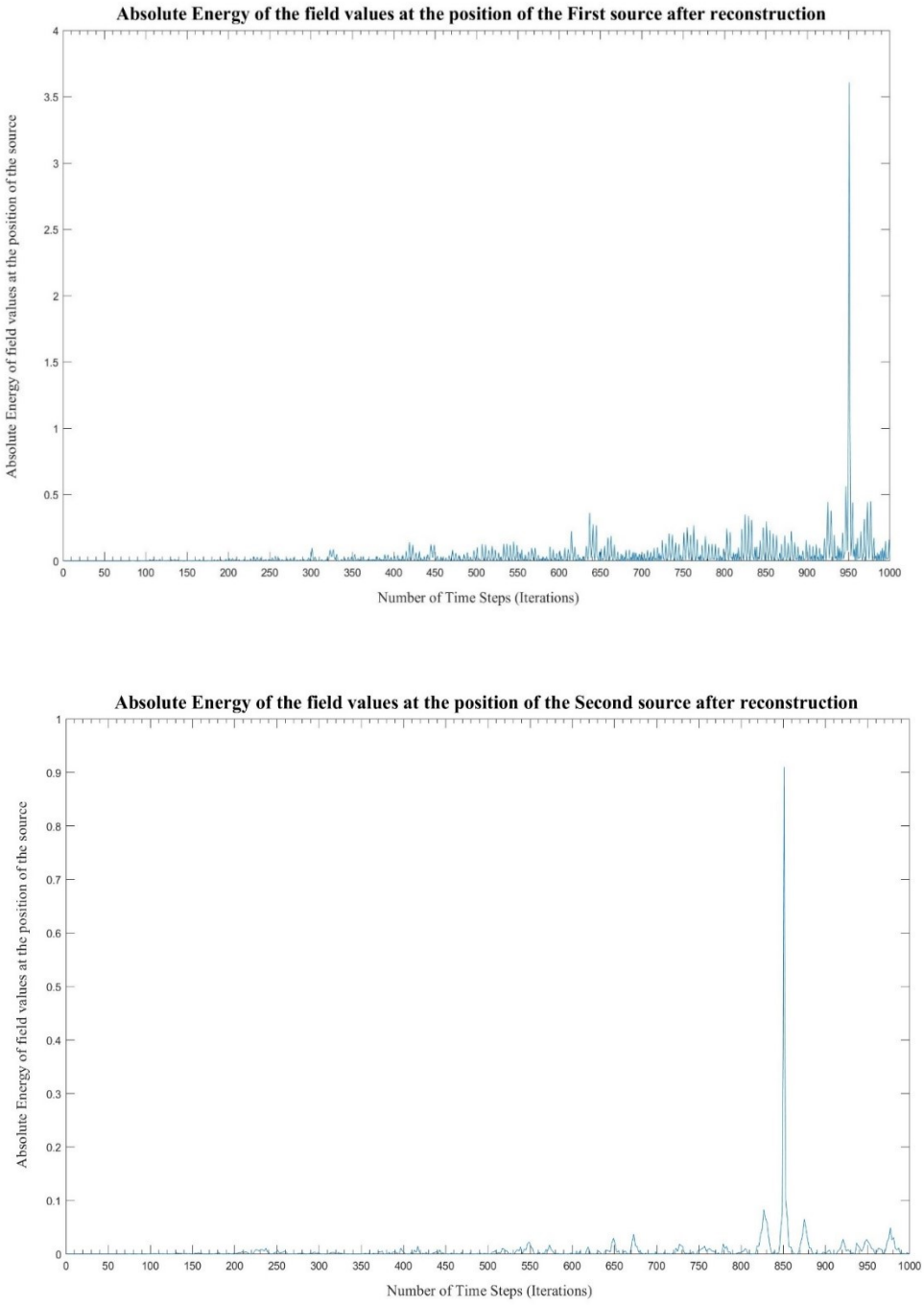

Figure 4.4 The absolute energy of the two reconstructed sources excited at different time intervals indicating the peak as the Maximum Energy.

4.3.2 Space Focusing Gain

The second parameter that is discussed is called the Space Focusing Gain (SFG). This is used to characterise the space focusing property of time reversal. This parameter is defined as the ratio between the maximum energy of the field values at the position of the reconstructed source to the maximum energy of the field values at a point situated very far from the reconstructed source [20]. This parameter is similar to the Signal to Noise ratio (in space) of the signal in that it describes the strength of the reconstructed source compared to a non-source point located far from the source, characterizing the noise. If R_s is the location of the reconstructed source and R_{NS} is a non-source point located very far from S, then SFG is given by [21]

$$SFG = \frac{Max(R_s)}{Max(R_{NS})} \dots\dots (35)$$

4.3.3 Signal to Noise Ratio in time

The Signal to Noise Ratio in time (SNRt) is used to describe the strength of the time focusing property of time reversal. It is the ratio of the Maximum energy of the field values in a time interval that contains the reconstructed source to the RMS value of the field values taken in an interval that contains the non source noise values characterising the noise [21]. If R and t describe the position and time of the field point, then SNRt is given by [21]

$$SNRt = \frac{\max_{t \epsilon N_S}(|E_z(t,R)|^2)}{< (|E_z(t,R)|^2) > t \epsilon N_{NS}} \dots\dots (36)$$

Where, N_S represents the time duration that contains the reconstructed source, and N_{NS} represents the time duration of the non-source noise positions.

4.4 PERFORMANCE OF THE CONVENTIONAL TIME REVERSAL

This section analyses the performance of time reversal in regard to the reconstruction of multiple sources. The characteristics of the reconstructed sources described in Section 4.3 is compared to different parameters such as the total number of iterations in the FDTD algorithm, the number of output probes used in the reinjection of the time reversed fields, the distance between the output probes and the sources. A cavity with 100 FDTD cells in the *x*- and the *y*-direction, surrounded by PEC walls to ensure that multipaths are chosen for the following analysis. An impulse source and a Gaussian source of frequency of 10GHz with an initial delay of 10 times its spread τ are used for the excitation purpose. The Gaussian source that is used is shown in Figure 4.5. The characteristics are compared for both the impulse and Gaussian sources.

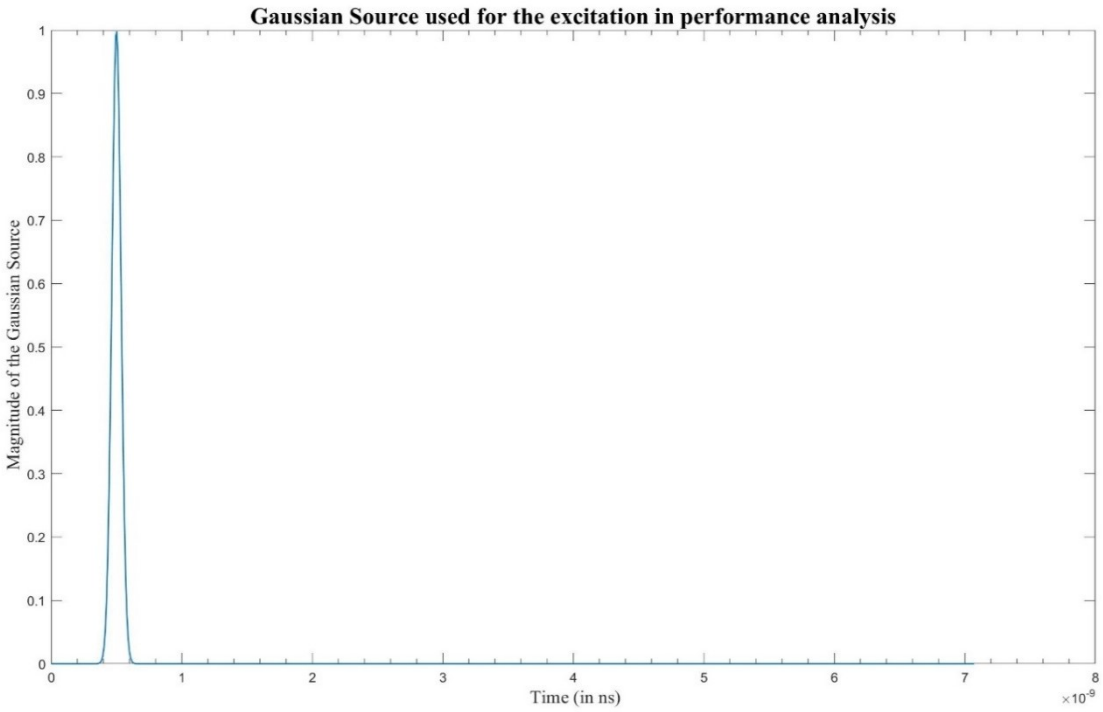

Figure 4.5 Gaussian Source used for the excitation

4.4.1 Number of Iterations

The cavity is first excited by three Gaussian sources shown in Figure 4.5. The field values recorded at four output nodes are reversed in time and reinjected back into the cavity as shown in Figure 4.6 (a) and Figure 4.6 (b). Figure 4.6 (c) shows the magnitude of the field values at their original locations for all the time steps of reinjection. The maximum energy of the field at the position of the reconstructed sources is compared to the total iteration taken between 200 iterations to 15000 iterations of the FDTD simulation. The same procedure is repeated for three impulse sources excited at the same positions. Figure 4.6 (d) clearly shows that the maximum energy of the reconstructed sources increases exponentially with the increase in the number of simulations for both the type of sources. A higher simulation runtime characterized by a higher number of iterations allows for more multipaths on the source inside the cavity. As a result, the three sources have more energy with the increase in the number of iterations.

The space focusing gain of the two types of sources is compared with the number of iterations. Figure 4.6 (e) indicates a weak relationship between the number of iterations and the space focusing gain; there is no significant change as the iterations increase for both types of the sources.

Forward Propagation of source at time step=60

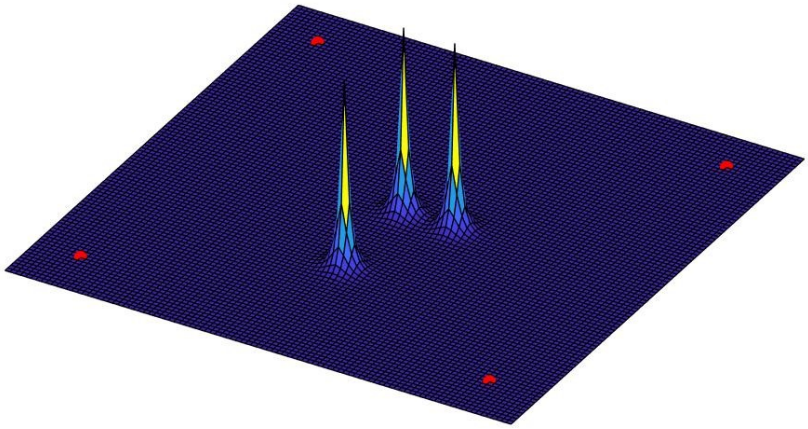

(a)

Reinjection from four output nodes at time step=18

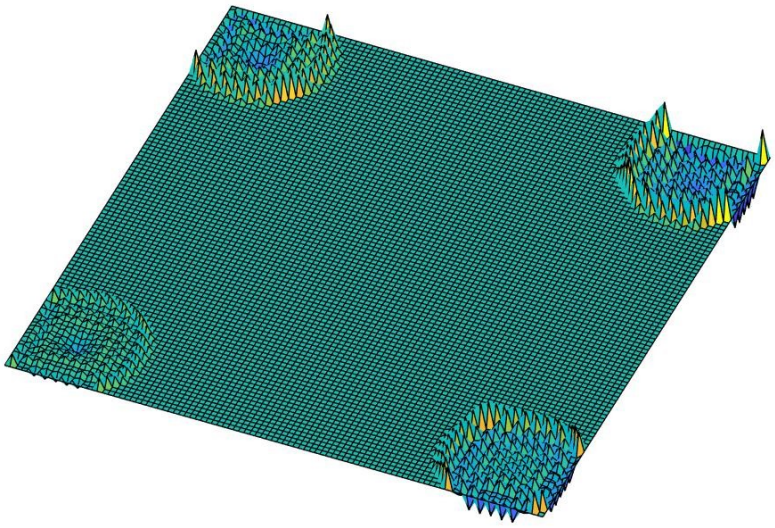

(b)

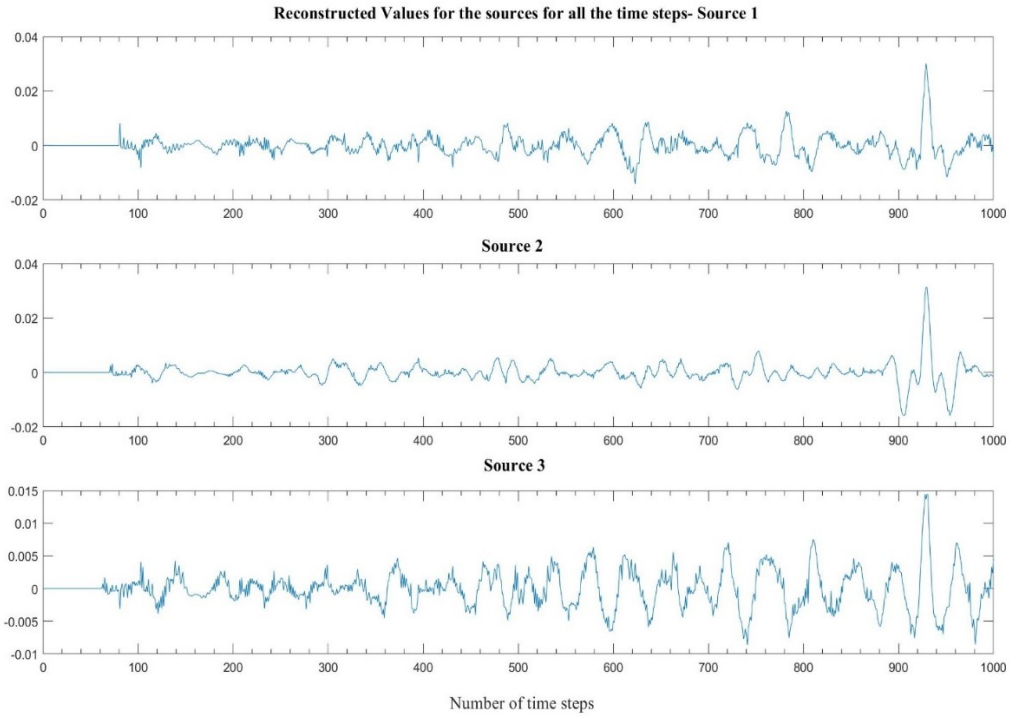
Reconstructed Values for the sources for all the time steps- Source 1
Source 2
Source 3
Number of time steps

(c)

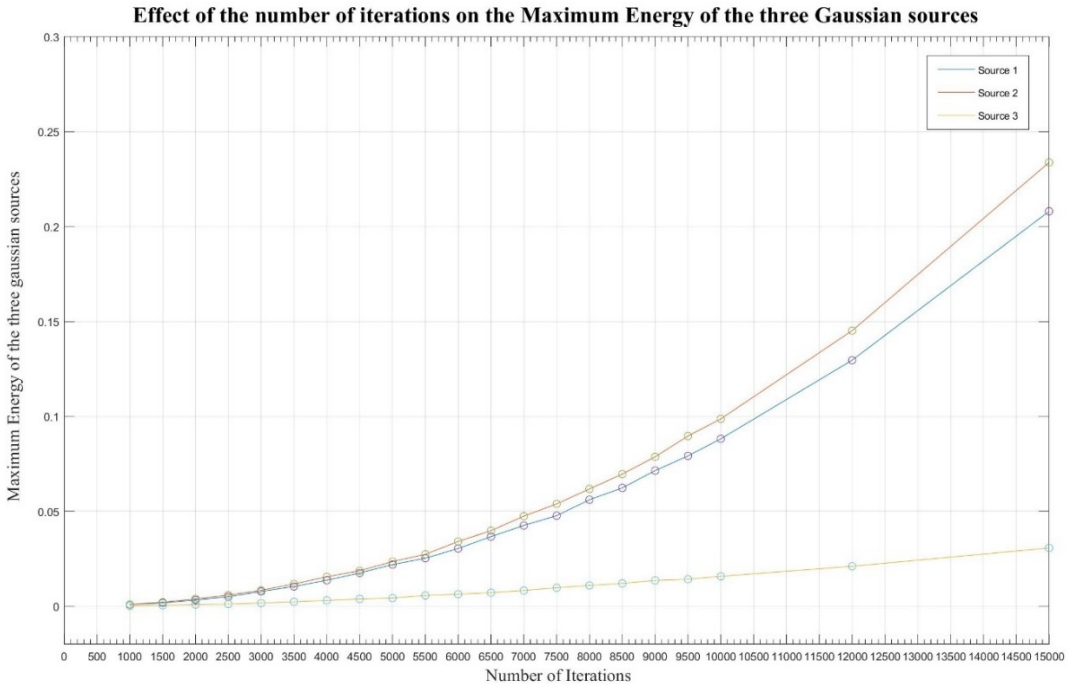
Effect of the number of iterations on the Maximum Energy of the three Gaussian sources
Source 1
Source 2
Source 3
Maximum Energy of the three gaussian sources
Number of Iterations

(c)

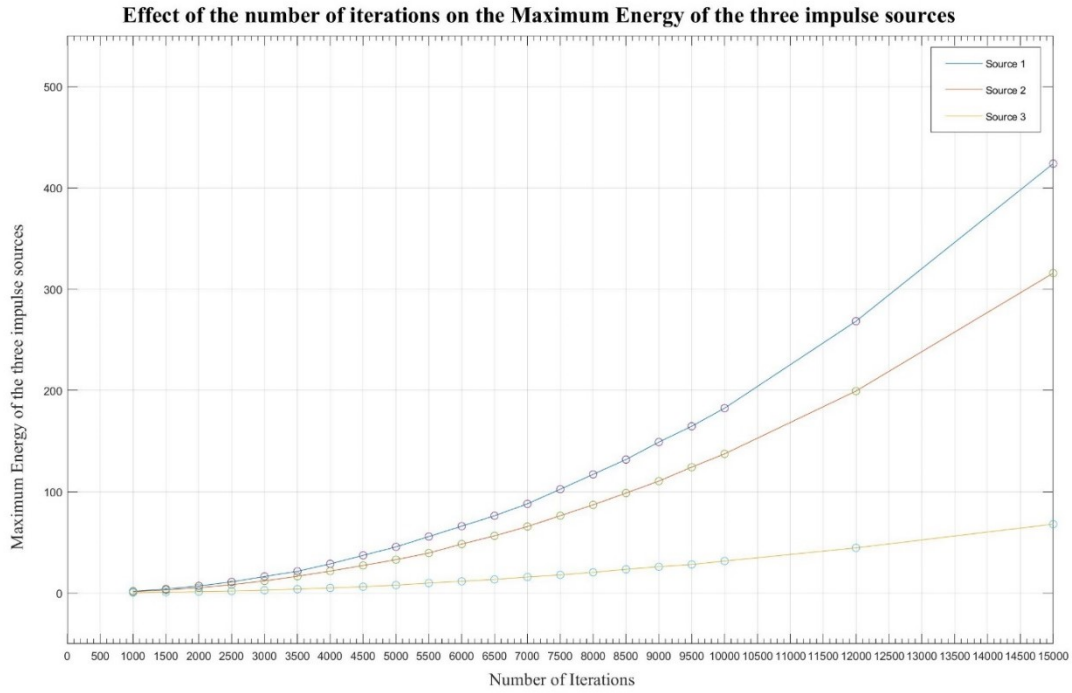
Effect of the number of iterations on the Maximum Energy of the three impulse sources
Source 1
Source 2
Source 3
Maximum Energy of the three impulse sources
Number of Iterations

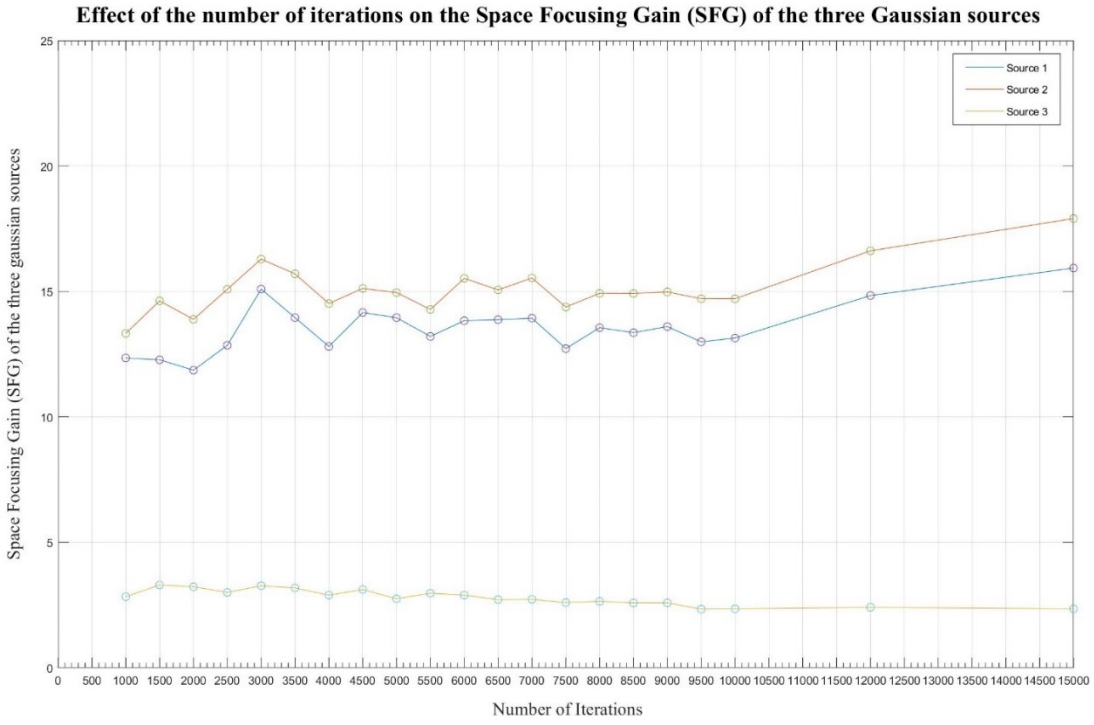
Effect of the number of iterations on the Space Focusing Gain (SFG) of the three Gaussian sources
Source 1
Source 2
Source 3
Space Focusing Gain (SFG) of the three gaussian sources
Number of Iterations

(d)

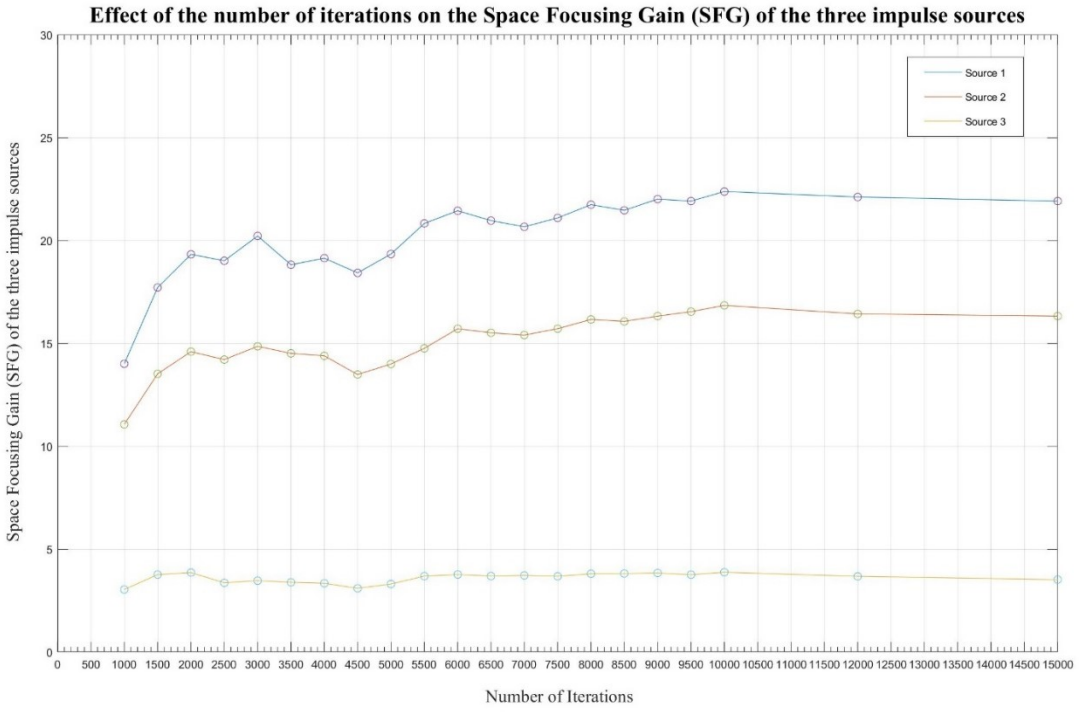

(e)

Figure 4.6 (a) PEC cavity excited by three Gaussian sources with four output probes after the delay in the excitation source (b) Recorded fields are reversed in time and reinjected back into the cavity from the four output probes. (c) The magnitude of the reconstructed sources for all the iterations with peaks indicating the source (d) Effect of the number of iterations of the FDTD-Time reversal algorithm on the maximum energy of the three reconstructed sources for Gaussian and impulse sources. (e) The number of iterations on the Space focusing gain on the three sources.

The next metric for comparison is the signal to noise ratio in time (STRt) of the three sources. Similar to the SFG relation, the signal to noise ratio in time does not show a drastic change for increasing iterations as shown in Figure 4.7. Although the STRt has a slightly higher value for the 1000^{th} to 1500^{th} iteration, it does not indicate an optimal iteration value. The STRt's for these iteration numbers is slightly higher because the number of iterations in the FDTD algorithm given the number of FDTD cells in both the direction- 100 in this case- is not sufficient for the optimal travel distance needed for the EM waves to cover. As the number of iterations, i.e. the number of multipaths increase, the STRt does not show a significant change, thereby indicating an optimum iteration number for the time reversal algorithm.

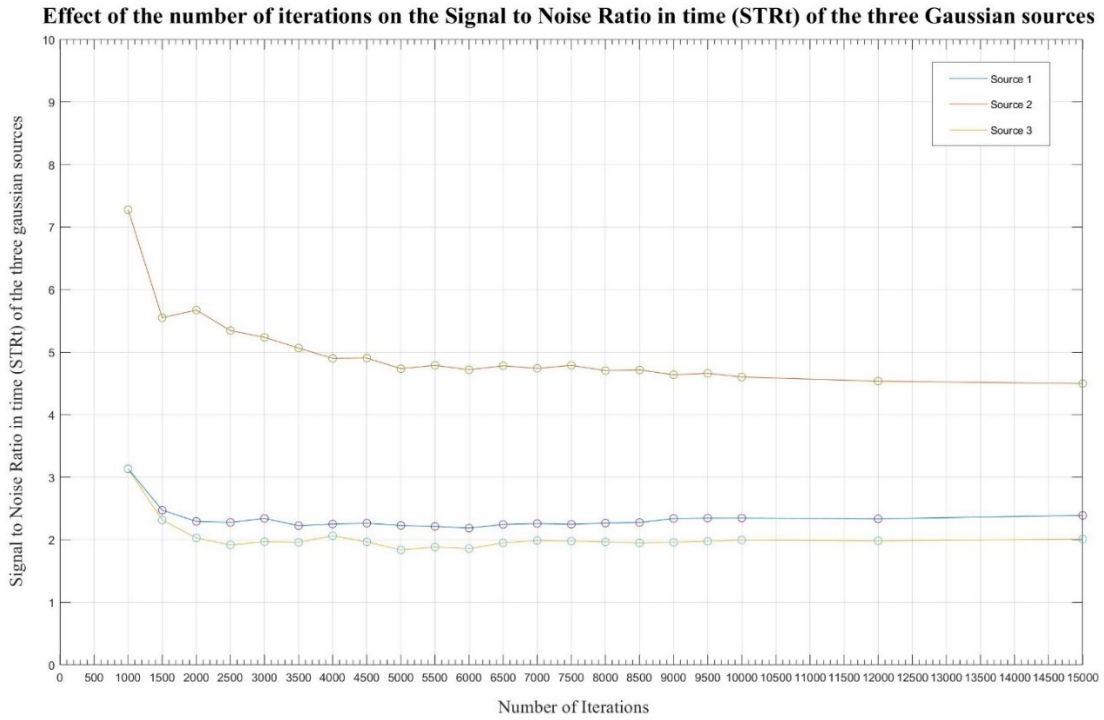
Effect of the number of iterations on the Signal to Noise Ratio in time (STRt) of the three Gaussian sources
Signal to Noise Ratio in time (STRt) of the three gaussian sources
Number of Iterations
Source 1
Source 2
Source 3
0
1
2
3
4
5
6
7
8
9
10
0 500 1000 1500 2000 2500 3000 3500 4000 4500 5000 5500 6000 6500 7000 7500 8000 8500 9000 9500 10000 10500 11000 11500 12000 12500 13000 13500 14000 14500 15000

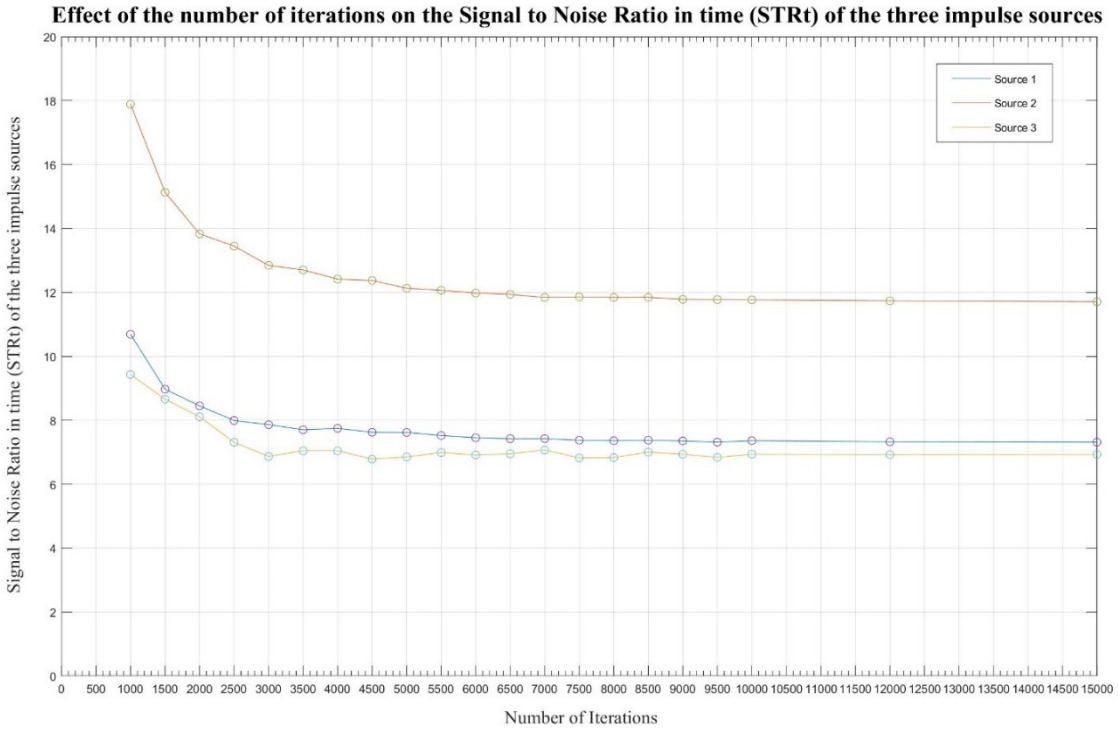

Figure 4.7. The number of iterations on the signal to noise ratio (STRt) on the three sources.

4.4.2 Number of output nodes

The same PEC cavity is excited three Gaussian sources and then with three impulse sources similar to the previous section. A total of 32 output nodes surround the three sources as shown in Figure 4.8. The analysis with regard to the number of output nodes is performed by first activating only one of the output nodes for a total of 3000 iterations. The following simulations are carried out with the addition of one more output node, and the process is carried out for the total number of output nodes selected with the same number of iterations. This depicts the behaviour of the time reversal algorithm with the increasing number of output nodes.

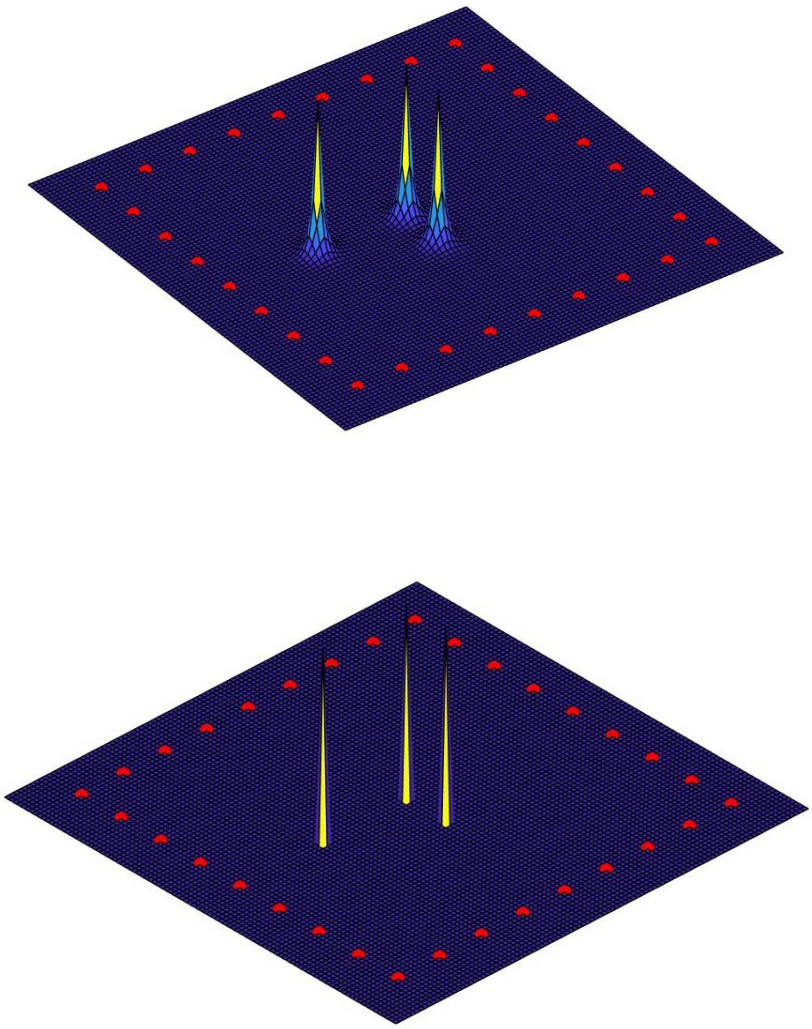

Figure 4.8. PEC cavity excited by three impulse and Gaussian sources surrounded by 32 output probes.

The maximum energy of the two types of sources is plotted for increasing number of output probes as shown in Figure 4.9. It can be seen that with increasing output nodes, the maximum energy of both types of sources increases almost exponentially.

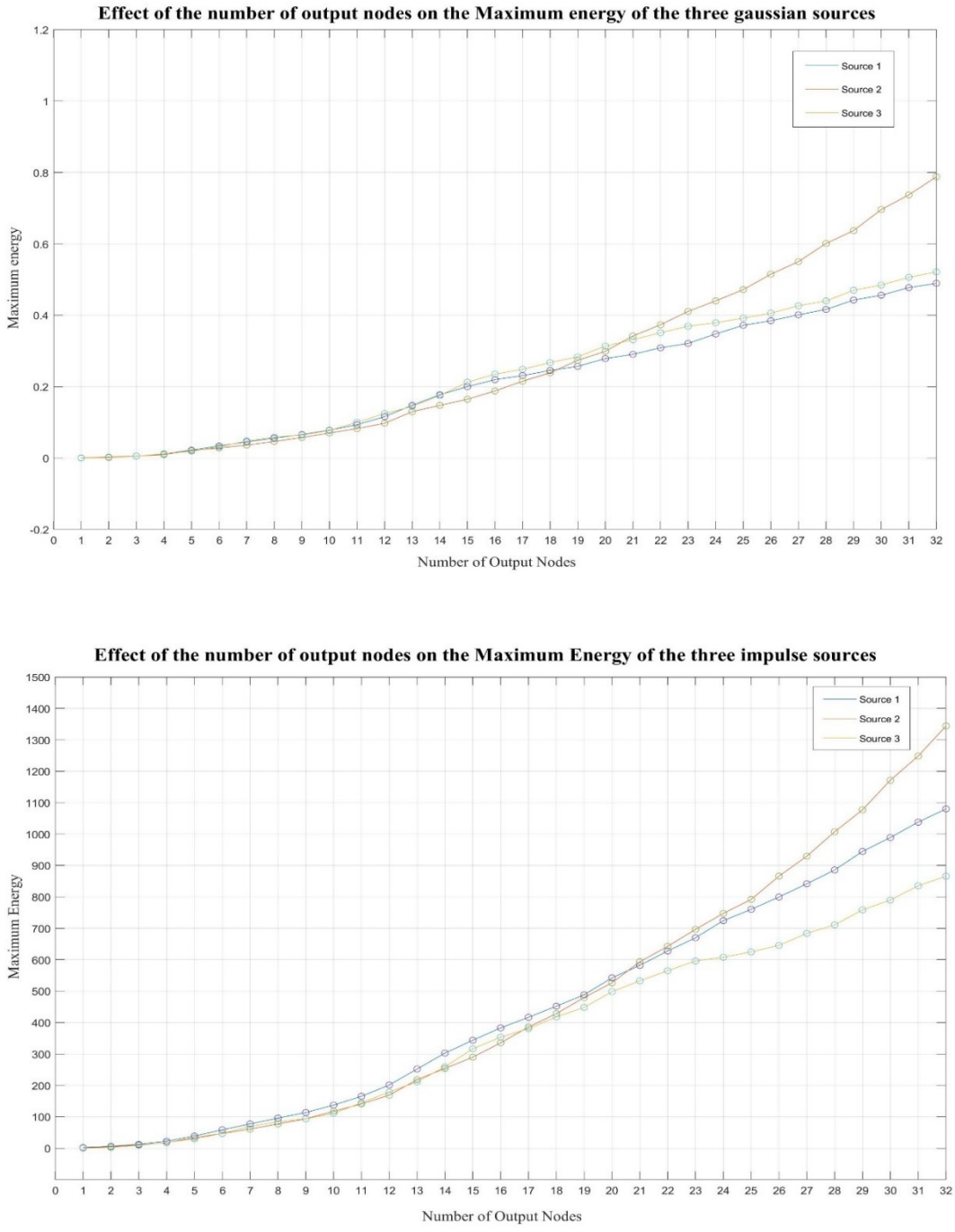

Figure 4.9 Variation in the maximum energy of the reconstructed sources due to the addition of output probes.

The space focusing gain is now considered for the comparison with the increasing number of output nodes. Figure 4.10 indicates that with each addition of an output node, the space focusing gain increases up to a certain number of output nodes and exhibits a weak dependence with each addition after that. Increasing output nodes helps in adding more information regarding the source until a point where no new information about the source can be added leading to the weak dependence after the addition of the 24^{th} probe for both the types of sources.

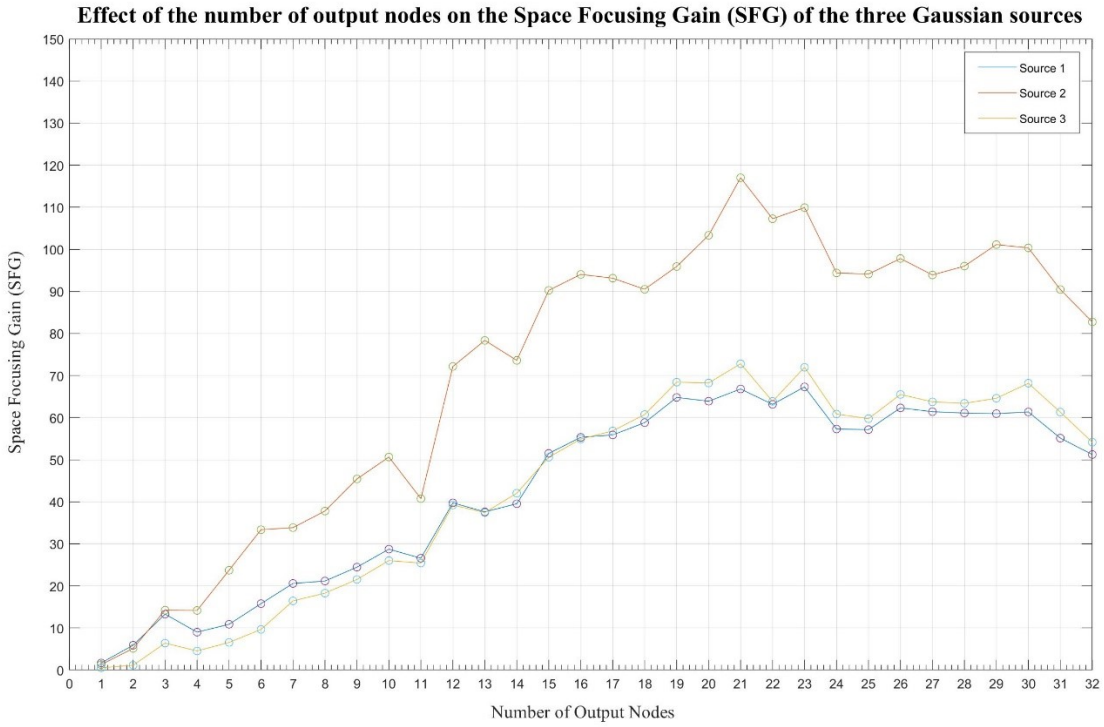

(a)

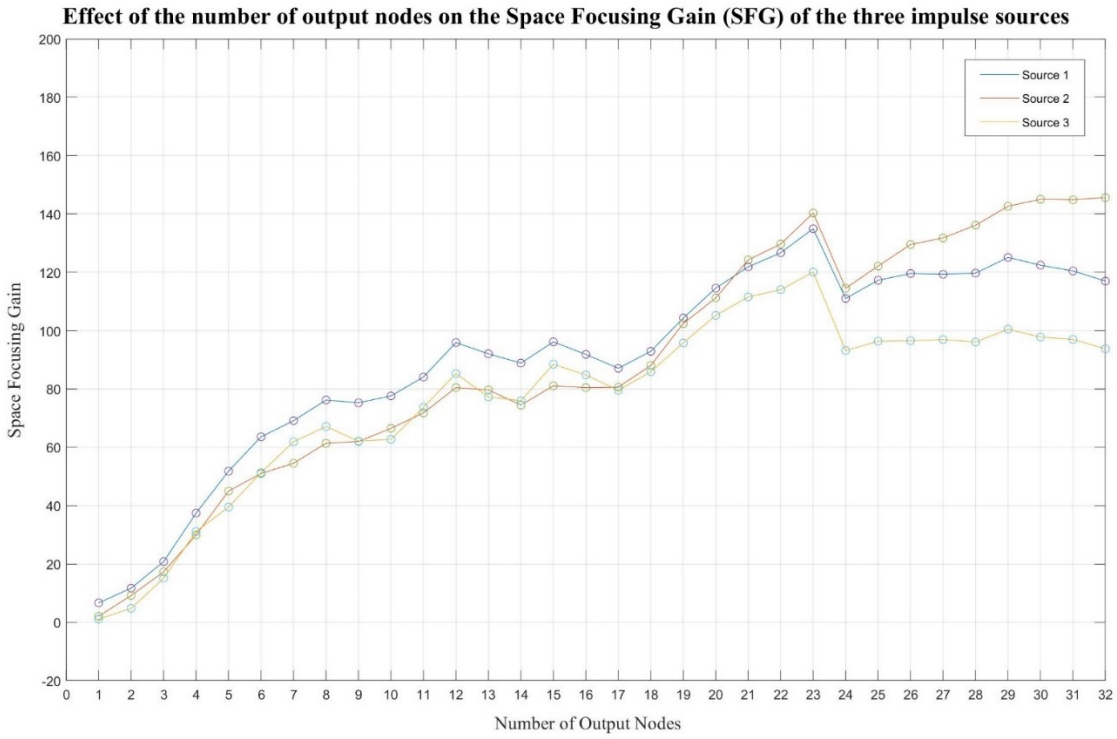

(b)

Figure 4.10 (a) & (b) Number of output nodes on the space focusing gain of both the Gaussian and the impulse sources.

The Signal to Noise Ratio (STRt) in time is now compared with the addition of output nodes in Figure 4.11. The STRt as seen in Figure 4.11 does not show a significant increase or decrease with the addition of more output nodes. The number of iterations that is used for all of the performance analysis is 2000. The reason for the relatively higher or lower values compared with the following values with the addition of the second to the fourth probe is due to limited information offered by a low number of output nodes in the said simulation run time. With each addition of output probes after enough information about the source is received by the nodes, the STRt does not change very much, staying in a small range as seen in the figures.

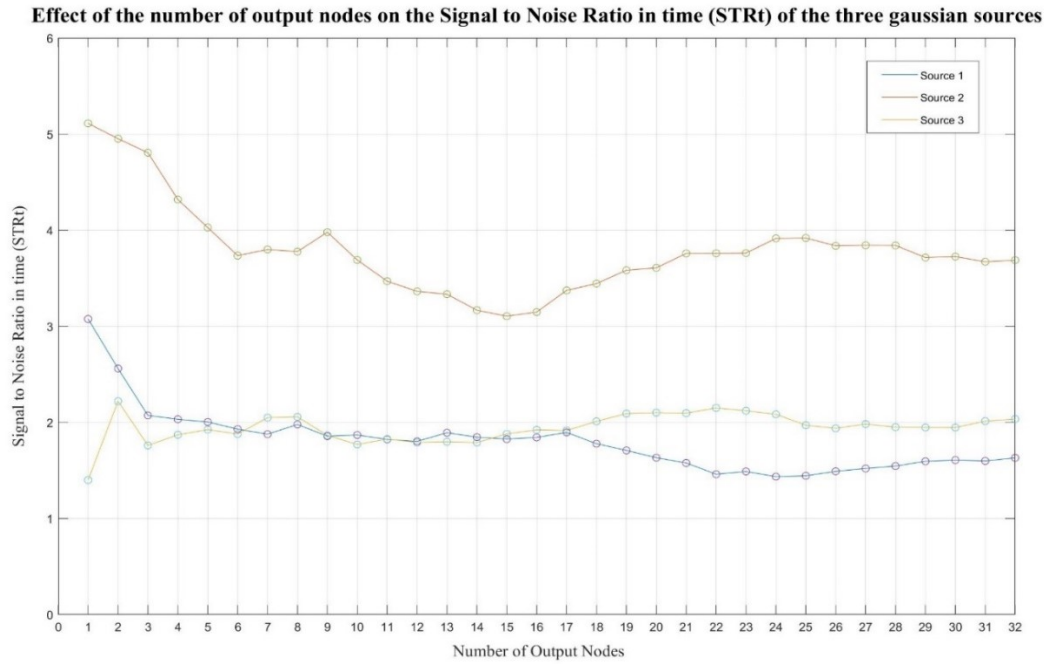

(a)

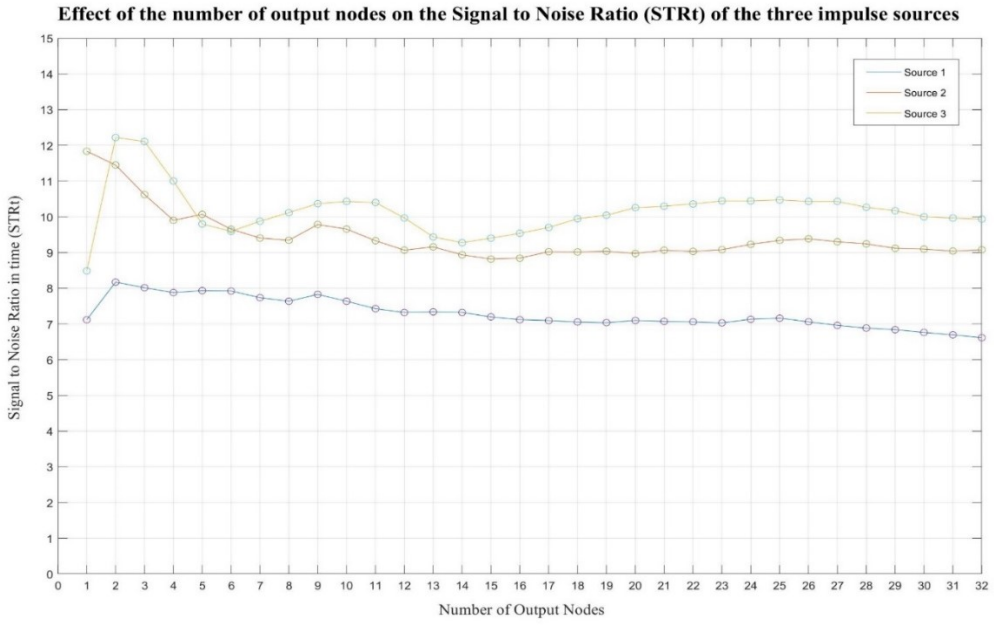

(b)

Figure 4.11 (a) & (b) Number of output probes on the signal to noise ratio in time of the reconstructed sources.

4.4.3 Proximity of the output nodes

For the relationship between the characteristics of the reconstructed source and the proximity of the output node, A single Gaussian source is excited in the center of the same PEC cavity used in the chapter. The previous two sections have established that the results of the performance analysis of time reversal are consistent for both impulse and the Gaussian source. Hence, this section will use only the Gaussian source to establish the relationship between the proximity of the output nodes and the source. The number of FDTD cells in each direction is 100. This Gaussian source is reconstructed with the help of six output nodes that are placed around the source. The proximity relation is realised by changing the said distance between the source and the output nodes. In the simulation for this section, the distance between the source and the output nodes is changed from 5 cells to 40 cells with an addition of one cell in each case. Figure 4.12 shows the positions of the centrally places Gausian source, the output nodes- red dots- and the direction of increase in the direction-green arrows- between the two components.

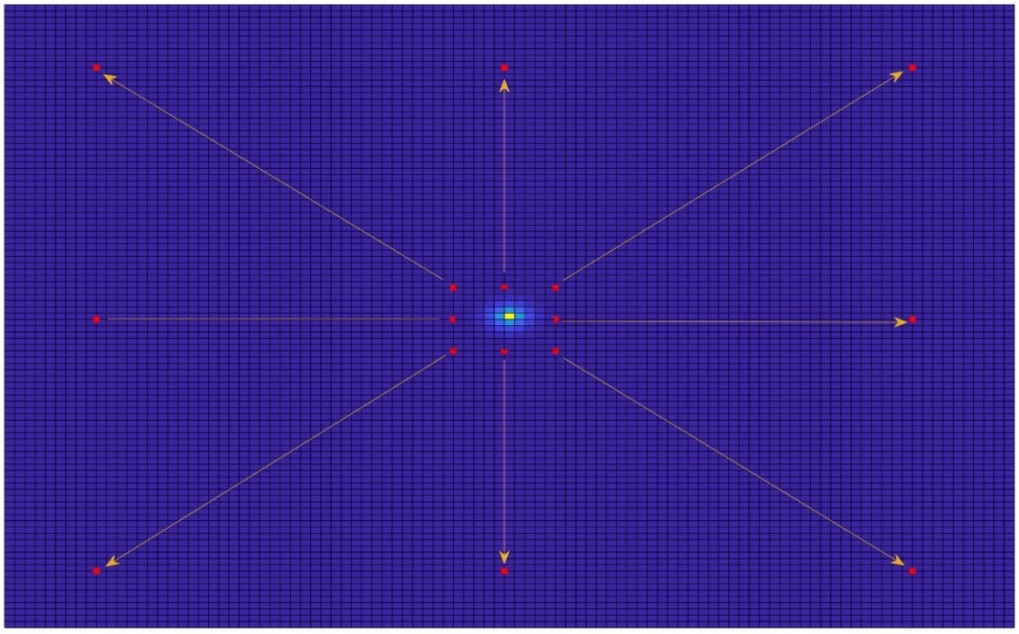

Figure 4.12 The direction of the movement of the output probes for changing the proximity

Similar to previous sections, the maximum energy of the source, the space focusing gain and the signal to noise ratio in time are compared with the distance between the output nodes and the source. Figure 4.13 shows that the maximum energy of the centrally placed source is unaffected by the change in the distance between the output nodes and the source. This conforms to the results of the previous sections where the maximum energy showed an increase with increasing number of iterations and output nodes. Here, the number of iterations and the output nodes is fixed for the entirety of the simulation. Therefore, the maximum energy does not undergo any change when the position o the output probes are changed.

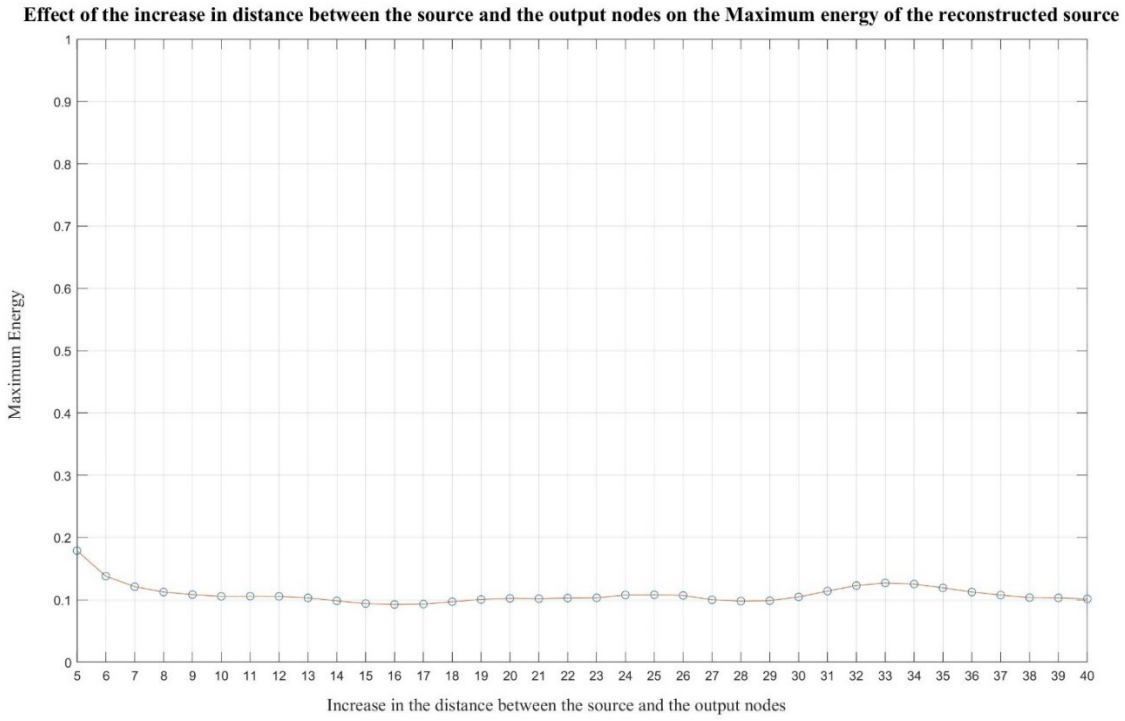

Figure 4.13 Changes in maximum energy when the distance between the source and the output nodes are changed

The signal focusing gain is plotted against the increasing distance between the source and the output nodes in Figure 4.14. It can be seen that the SFG reduces exponentially with increasing distance with no significant change after a particular increase in distance.

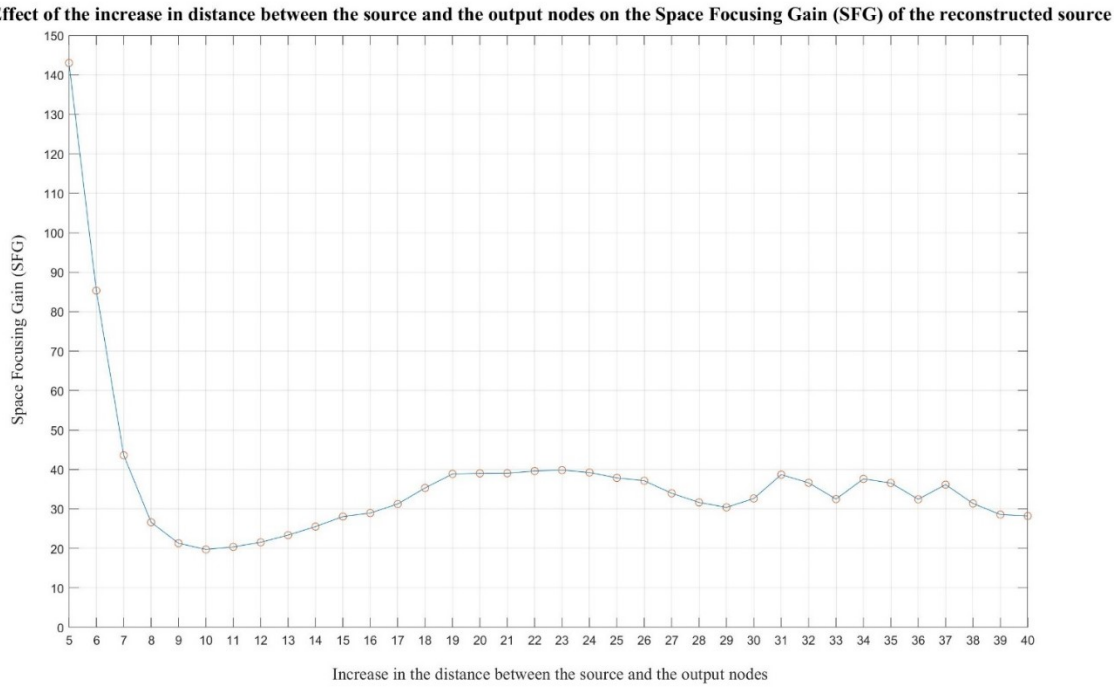

Figure 4.14 Space focusing gain plotted against the increasing distance between the source and the output nodes.

Figure 4.15 shows the variation in the STRt for the different distances between the source and the output nodes. Similar to the case of maximum energy, the STRt does not show any variations with the increasing distance, the values of STRt for this configuration stays within a small range as seen in Figure 4.15.

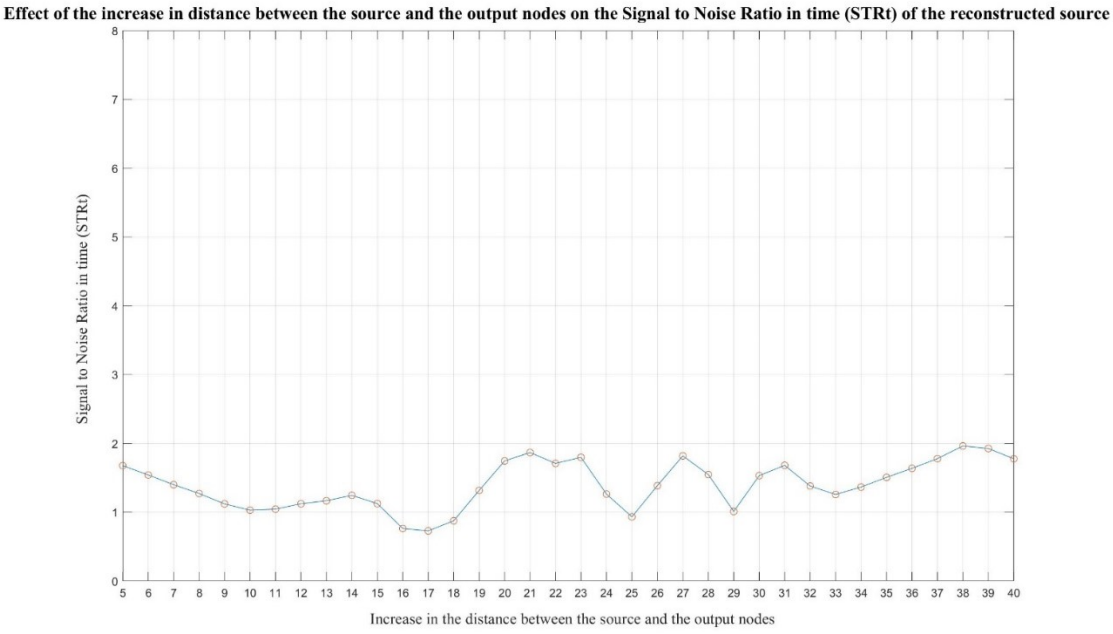

Figure 4.15 Variation of the STRt of the reconstructed sources with increasing distance between the source and the output nodes.

4.5 SUMMARY

The characteristics of the reconstructed sources were analysed with changing parameters such as the number of iterations, number of output nodes and the proximity of the output nodes. The results of impulse and Gaussian sources were compared to ensure consistency in the results. The maximum energy shows a strong dependence on the number of iterations and the output probes but not with the changing proximity of the output nodes. The SFG and STRt, on the other hand do not depend strongly on the changing iterations and output nodes, reaching an almost constant level after a certain point. Similarly, the STRt does not depend too much on the proximity of the output nodes, but the SFG shows a sharp decrease and an almost constant behaviour. This indicates the time reversal can be performed with a limited number of iterations and output nodes at an optimal distance for reliable reconstruction of sources.

Chapter 5 RECOVERY OF MAGNITUDE OF SOURCES AFTER RECONSTRUCTION

The time reversal algorithm used in the previous sections is accurate in locating the positions of the sources, but it fails to recover the original magnitude of the sources. The following sections elaborate and analyses a method that is successful in recovering the original magnitudes of the sources. Section 5.1 demonstrates the failure of the conventional FDTD algorithm in recovering the magnitude. Section 5.2 details the method based on regularized least squares [17] which is used as a fix to the said limitation. The next section aims to eliminate the limitation of conventional time reversal using [17] and elaborates on its limitations. The final section explores a potential fix to the said limitations using the elastic net [23].

5.1 FAILURE IN RECOVERY OF MAGNITUDE OF CONVENTIONAL TIME REVERSAL ALGORITHM

Three impulse sources with unit magnitude are excited after a delay in the cavity that has been used in the previous sections. The FDTD simulation is run for a total of 3000 iterations. Figure 5.1 shows the magnitude of the three sources after the reconstruction takes place. The figure indicates that though the location of the sources is recovered, there is a lot of error in its magnitude. This recovered magnitude increases with the number of iterations as explained in Section 4.4.1 and does not recover the original magnitude.

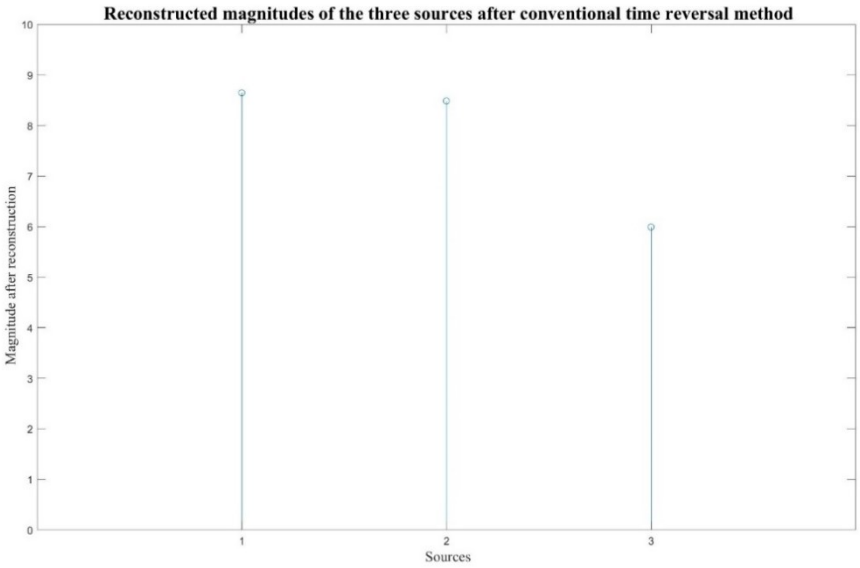

Figure 5.1 Reconstructed magnitude of the three impulse sources after conventional time reversal

5.2 ACCURATE RECOVERY OF THE MAGNITUDE OF THE SOURCES

An important relation is derived that serves as a necessary condition for the reconstruction for multiple sources in [18]. Individual backward transmission from different output probes is performed by the authors as opposed to activating all the output probes at once in conventional time reversal. This method offers equality between the energy of the signal at each output node and the sum of the values at each source node at the end of each backward propagation as shown in the below equation. [18]

$$\sum_{n=0}^{N-1} Y_j^2[n] = \sum_{i=1}^{I} a_i S_i^j[N-1] \dots\dots (37)$$

In the above equation, Y_j represents the energy of the field values taken at the jth output node-for J=1,2, 3……J output nodes- after the jth backward transmission with N representing the total number of time steps. S_i^j represents the final value of the ith input node after the jth backward transmission with I= 1,2, 3…….I input nodes and a_i representing the magnitudes of the original sources.

This equation can be converted to a system a linear equation with each equation representing the above relation for one particular backward transmission. This system contains the number of equations equal to the number of output nodes and the number of unknowns being different points selected from the computational domain at random. [18]

$$\begin{bmatrix} S_1^1 & \cdots & S_N^1 \\ \vdots & \ddots & \vdots \\ S_1^J & \cdots & S_N^J \end{bmatrix} \begin{bmatrix} a_1 \\ \vdots \\ a_N \end{bmatrix} = \begin{bmatrix} \sum_{m=0}^{M-1} y_1^2[m] \\ \vdots \\ \sum_{m=0}^{M-1} y_J^2[m] \end{bmatrix} \dots\dots (38)$$

The above equation is the matrix form of the equation described earlier in the section. The first (S) matrix is an N x J matrix that contains N rows of points selected at random from the cavity and J columns that represents J backward transmissions from J output probes. The second matrix is an N x 1 vector containing the magnitudes of the original sources. The matrix on the right side is a J x 1 vector containing the energies of J individual back transmissions. This system is used for finding the value of the magnitude vector [a] as the [S] and [Y] are obtained from the simulation.

The number of points chosen is significantly larger than the number of output probes, i.e. the number of equations making it a system of undetermined equations [17]. This would mean an infinite number of solutions for the vector [a]. The accurate solution of the magnitudes of the sources is obtained with the help of finding a sparse solution for [a]. This is achieved by converting the above problem into a minimisation problem for obtaining the sparse solution as shown below. [17]

$$min(\|[S][a] - [Y]\|^2 + \lambda|a|) \dots\dots (39)$$

Here λ represents the parameter that controls the intensity of the constraint of the L1 norm. The optimal value of λ is discussed in the following sections.

[17] proposes the least absolute shrinkage and selection operator (LASSO) for the solution of the underdetermined set of equations and demonstrates its success. Section 5.3

elaborates on the success of using LASSO for the set up used in Section 5.1. The following sections are aimed at the limitations of using LASSO and the proposition of a new method.

5.3 ACCURATE MAGNITUDE RECOVERY USING LASSO

This section first elaborates on the new time reversal method detailed in [17]. Section 5.3.1 is used to explain the method using a flowchart. Section 5.3.2 demonstrates the reconstruction using LASSO for the accurate recovery of the sources. The limitations are then elaborated in Section 5.3.3.

5.3.1 Flowchart of the new time reversal method

Figure 5.2 depicts the flowchart of the new time reversal algorithm in detail. [17]

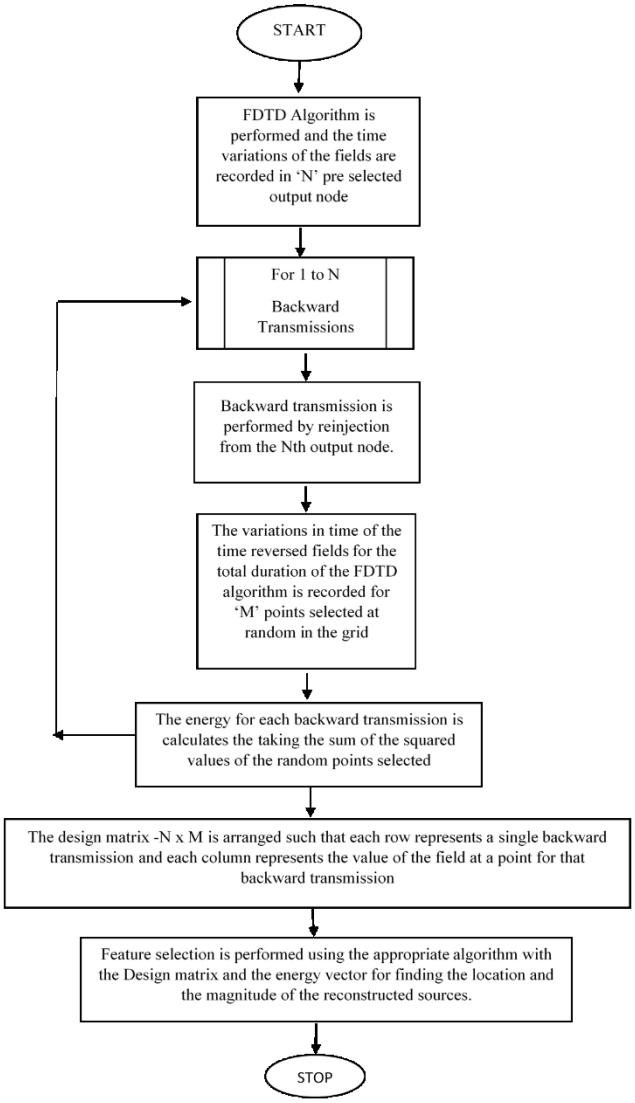

Figure 5.2 Flow of the new time reversal algorithm

In this method, the FDTD algorithm is performed twice similar to the conventional time reversal algorithm. The first FDTD is performed for the purpose of data collection from the output nodes for the total number of iterations. After the data collection is performed, the next FDTD differs from the conventional method. Backward transmissions are performed multiple times for the total number of output nodes. For 'N' output nodes, 'N' backward transmissions are performed and for each backward transmission, 'M' points are selected at random. The energy of each measurement is also recorded in a vector. Using the N x M design matrix and the energy matrix Y, the feature selection is performed. Although finding the magnitude of the sources involves solving the underdetermined system of equations described before, the problem is ultimately a feature selection problem and hence termed this way in Figure 5.2. LASSO is one of the algorithms that performs feature selection and is used for finding the magnitude of the sources.

5.3.2 Demonstration of lasso in magnitude reconstruction

The new time reversal algorithm is applied to the setup in Section 5.1. In the simulation, eight output nodes are used, and 3111 points are selected at random for each backward transmission. The total energies of the field values at the selected points are stored in another vector. An optimum value of 10^{-4} is selected for the λ parameter, and the LASSO is performed. Figure 5.3 shows the number of non-zeros of the vector given by the LASSO algorithm. These values point to the location of the original sources and give an accurate magnitude of the sources.

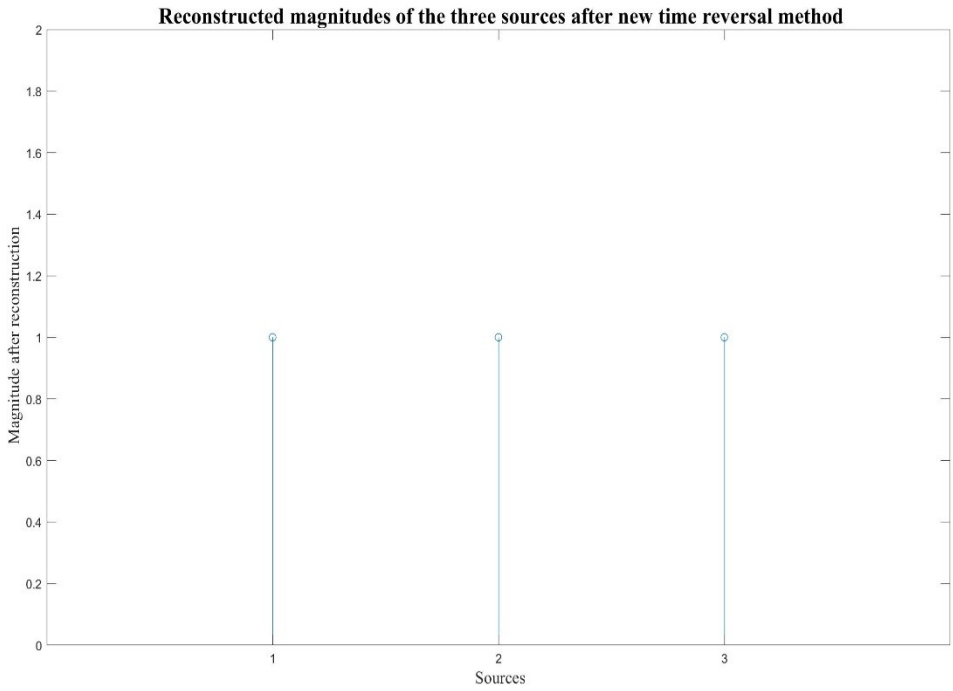

Figure 5.3 Magnitude recovery using the new time reversal method.

5.3.3 Optimal value of λ

The LASSO algorithm aims to minimize a cost function subject to the constraint of the feature vector having the least L1 norm. The L1 norm gives the sum of the absolute values of the feature vector [22]. The LASSO finds the vector with the least sum of the absolute value of the feature vector. It can be described as [22]

$$arg\ min_a(\|[S][a] - [Y]\|^2) + \lambda|a| \ldots\ldots (40)$$

Where S is the N x M design matrix with N rows corresponding to N output nodes and M columns representing M points chosen randomly in the grid. $|a|$ represents the L1 norm of the feature vector a which represents the magnitude of the sources. λ is the regularization

parameter that gives the intensity of the constraint that is placed on the cost function [25]for optimization.

If the original problem has k sources that need to be reconstructed then, ideally the feature vector a must contain k non-zeros terms out of M terms. This would make the vector a a sparse vector, and the L1 norm is highly effective in finding a sparse solution for underdetermined systems [22]. Hence the LASSO which places a constraint of the minimum L1 norm is used in [17] to get the magnitude of the reconstructed sources. An essential step in applying the LASSO is selecting the right regularization parameter λ. There are several objective ways to find the optimal regularization parameter for optimization problems such as the information criterion for model selection, AIC [23], BIC [24] and k-fold cross-validation [25].

The LASSO is performed with the help of a MATLAB package called SpaSM [26] that contains functions for implementing such algorithms. The LASSO algorithm in this package gives the AIC criterion for different values of lambda used for the optimization. The optimal lambda is selected by choosing the lambda that corresponds to the minimum value of the AIC [24] [28]. Table 5.1 gives the AIC values for the wide range of lambda values used for the set up used in Section 5.3.2 with three impulse sources of unit magnitude and eight output nodes. The optimum lambda value with the least AIC value is highlighted in bold. The same procedure is followed for the following feature selection techniques.

Table 5.1 Optimum Lambda selection using AIC

LAMBDA	**AIC**
6.0527	8
5.0792	5.7133
0.5011	0.1491
2.4198 x 10^-15	**5.671 x 10^-29**
1.2711 x 10^-15	6.5722 x 10^-29
5.9445 x 10^-16	7.6957 x 10^-29
7.5018 x 10^-16	9.2297 x 10^-29
6.3170 x 10^-16	1.0617 x 10^-28
6.5745e x 10^-16	1.1944 x 10^-28

Using this optimum value of lambda, the LASSO is performed on the setup. Figure 5.4 shows the semi-log plot of the magnitudes of the sources given by the non-zeros in the feature vector and the lambda values. The optimal lambda value is shown in the dotted line. The points where the dotted line intersects the magnitude gives the reconstructed magnitude of the setup.

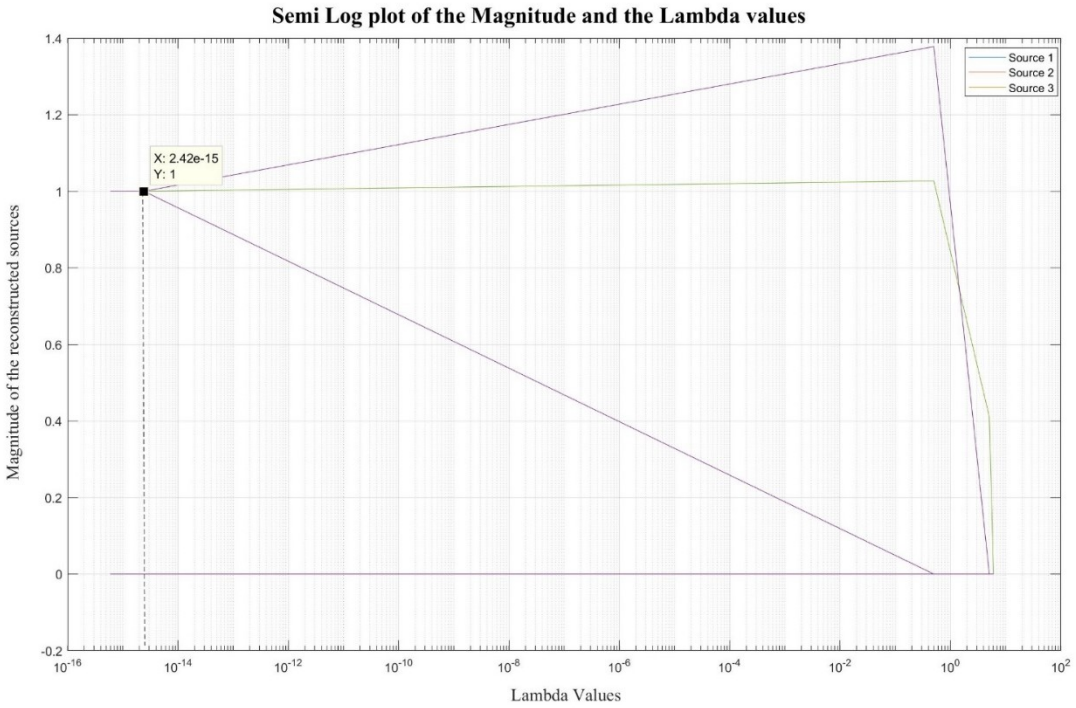

Figure 5.4 Magnitude and the lambda values with the optimum lambda

It can be seen that at the optimum value of the lambda parameter indicated by the dotted vertical line, the magnitudes of all the three sources is equal to one, that being their original magnitude.

5.3.4 Limitations of lasso in source recovery

The LASSO however has a significant limitation in its sparsity. The maximum that LASSO can recover is N non-zeros terms with N being the number of rows of the design matrix [25]. In the case of time reversal, the number of rows of the design matrix is the same as the number of output nodes used for the reinjection. If the number of sources is more than the number of output probes, then the LASSO algorithm only recovers the number of

sources equal to the output probes. This is illustrated by using six impulse sources and four output nodes. Figure 5.5 shows the semi-log plot of the magnitude and the lambda values. The optimum lambda values are found by the method used in section 5.3.3 and will also be used in the following sections. The first four sources as indicated by the legend are the only ones that are recovered. The other two sources overlap on the zero line. Hence only four out of six are reconstructed with the time reversal done using 4 output nodes.

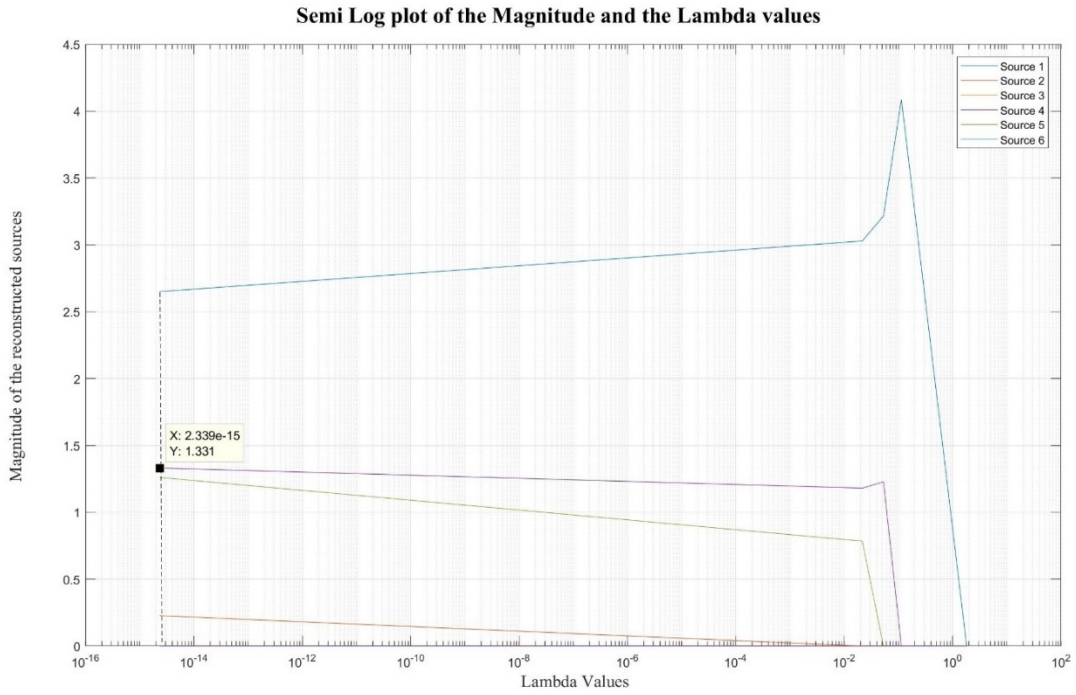

Figure 5.5 Magnitude and lambda values for the fail case of LASSO

Hence, LASSO is not the most suitable algorithm for the recovery of sources when the number of sources is not known. Another limitation with LASSO is the L1 penalty used in the optimization equation. Although the L1 penalty encourages sparsity in the extraction of the features, it can fail to represent the system when the sources are placed close to each other with the actual magnitude vector slightly denser than the sparse solution [25]. This limitation is illustrated with the help of a line of sources configuration as shown in Figure 5.6 (a). A set of 51 sources of equal magnitude are placed next to each other with eight output nodes. Besides the first limitation of reconstructing only a few of the sources, the

LASSO gives a very sparse solution with an increased magnitude not representative of the actual system. Figure 5.6 (b) compared the magnitudes of the original and the reconstructed sources after LASSO and clearly illustrates the limitation explained above.

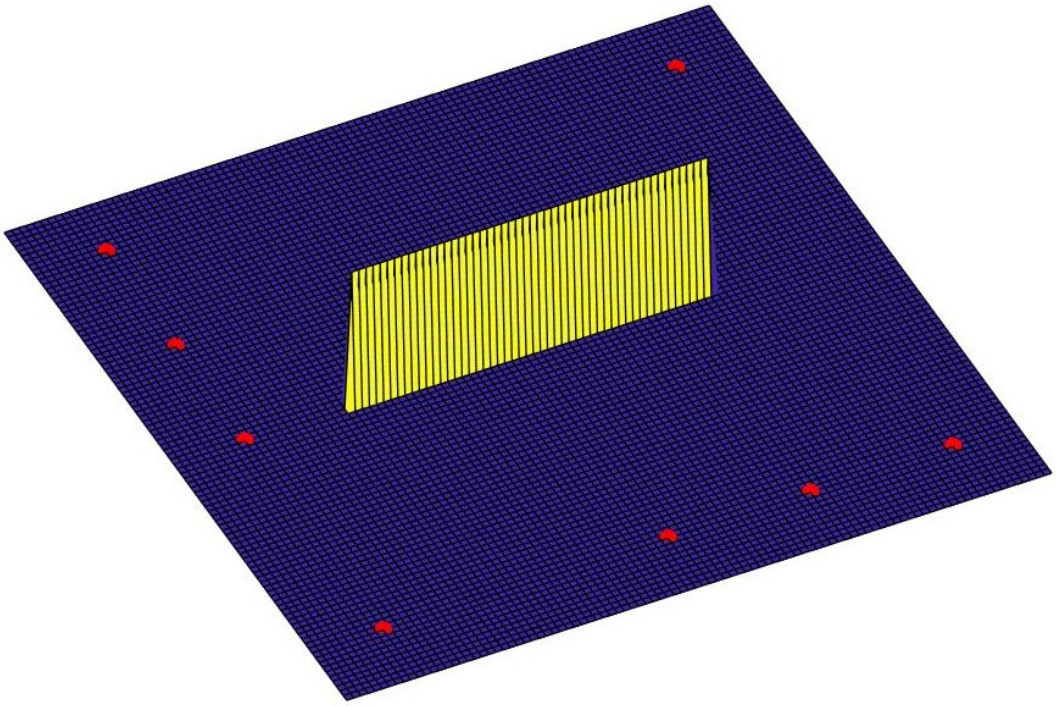

(a)

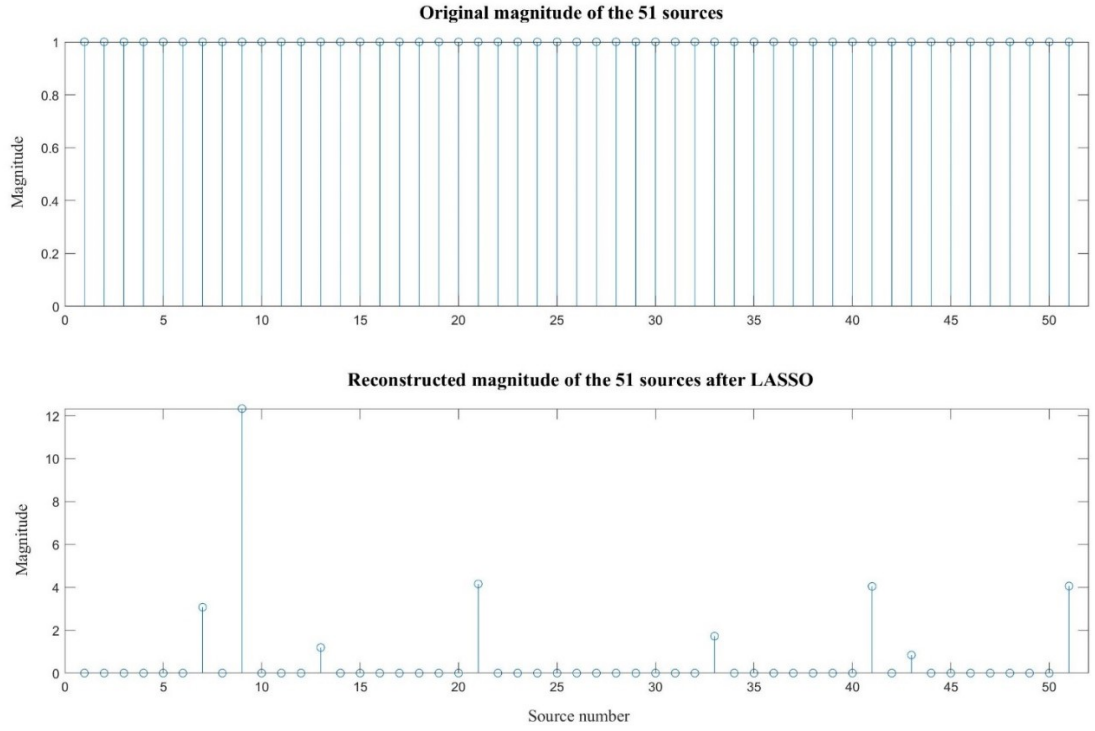

(b)

Figure 5.6 (a) Line of 51 sources with 8 output nodes (b) Comparison between the original and the reconstructed magnitude after LASSO time reversal.

5.4 POTENTIAL FIX FOR THE LIMITATIONS OF LASSO IN TIME REVERSAL

One way of trying to overcome the limitations of the LASSO in time reversal is to reduce the amount of sparsity in the vector containing the magnitudes. The constraint of having the smallest absolute value, i.e. the L1 norm can be replaced by the L2 norm. The L2 norm is the same as the distance between the vectors in Euclidian space. It is given by [27]

$$\|x\|_2 = \sqrt{x_1^2 + x_2^2 + x_3^2 + \cdots + x_N^2} \ldots\ldots (41)$$

For a vector of length N.

A constraint of minimizing the L2 norm would mean reducing the distance between two components of the vectors. This type of constraint would encourage density in the vector and could give solutions with non zero terms grouped together. This method of minimizing the L2 norm for feature selection is called the Ridge regression [27]. The ridge regression would encourage density rather than sparsity in the feature vector and would still not solve the problem detailed in the previous sections.

A balance between the density and the sparsity of the vector is required to solve the feature selection problem for time reversal. The Elastic Net [28] provides a common ground between the LASSO and the Ridge regression. The optimization problem using the elastic net is given by

$$arg\ min_a(\|[S][a] - [Y]\|^2) + \lambda_1\|a\|^2 + \lambda_2\|a\| \dots\dots (42)$$

Where λ_1 is the regularisation parameter that is responsible for the ridge regression and λ_2 is the regularisation parameter for the LASSO. If $\lambda_1 > \lambda_2$, then the feature vector is relatively denser than the LASSO solution and if $\lambda_2 > \lambda_1$, the feature vector is sparser than the ridge solution. The following sections use the elastic net algorithm for the fail cases of the LASSO and analyse its results.

5.4.1 Elastic net for the first limitation

The Elastic net is used for the configuration of six sources and four output nodes. The values of the magnitudes of the sources are compared for different values of λ_1 and λ_2. Figure 5.7 (a) to (d) plots the values of the magnitudes of the six sources one particular value of λ_1 and a range of values of λ_2. The optimum value of λ_2 is found by taking the value of lambda for the least AIC criterion. The simulation is performed for λ_1 values of 10^{-2}, 1, 50 and 500. The same SpaSM MATLAB toolbox [27] is used for implementing the elastic net. It takes the value of λ_1 as one of the arguments and calculates a range for λ_2.

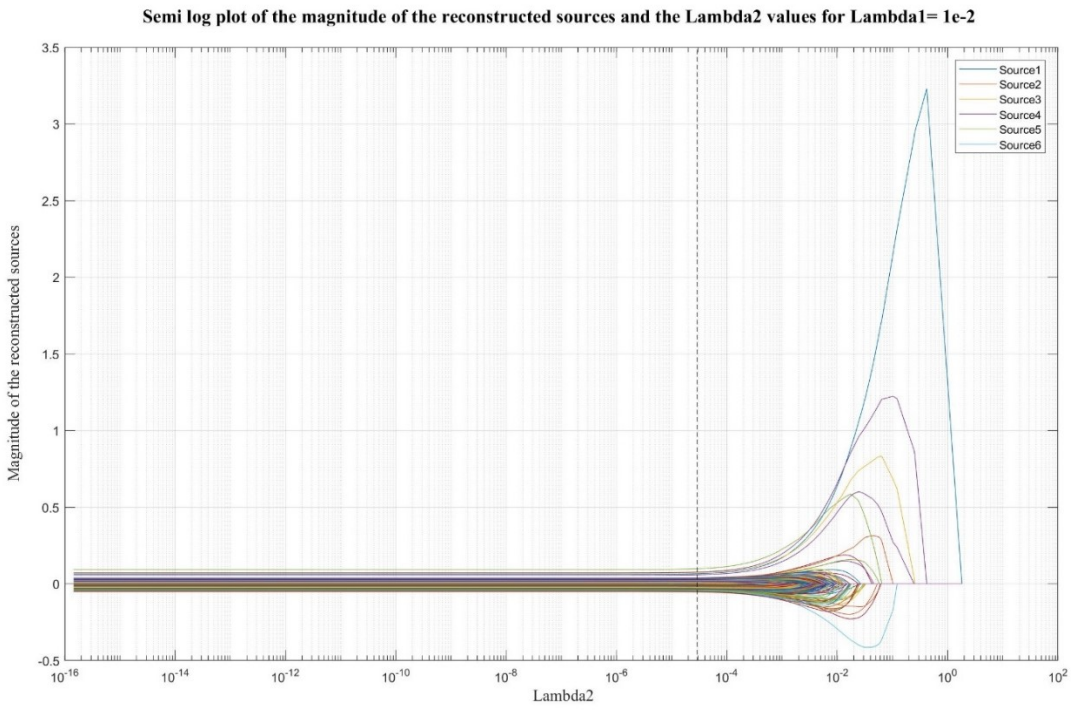

(a) Elastic net with λ_1=1e-2

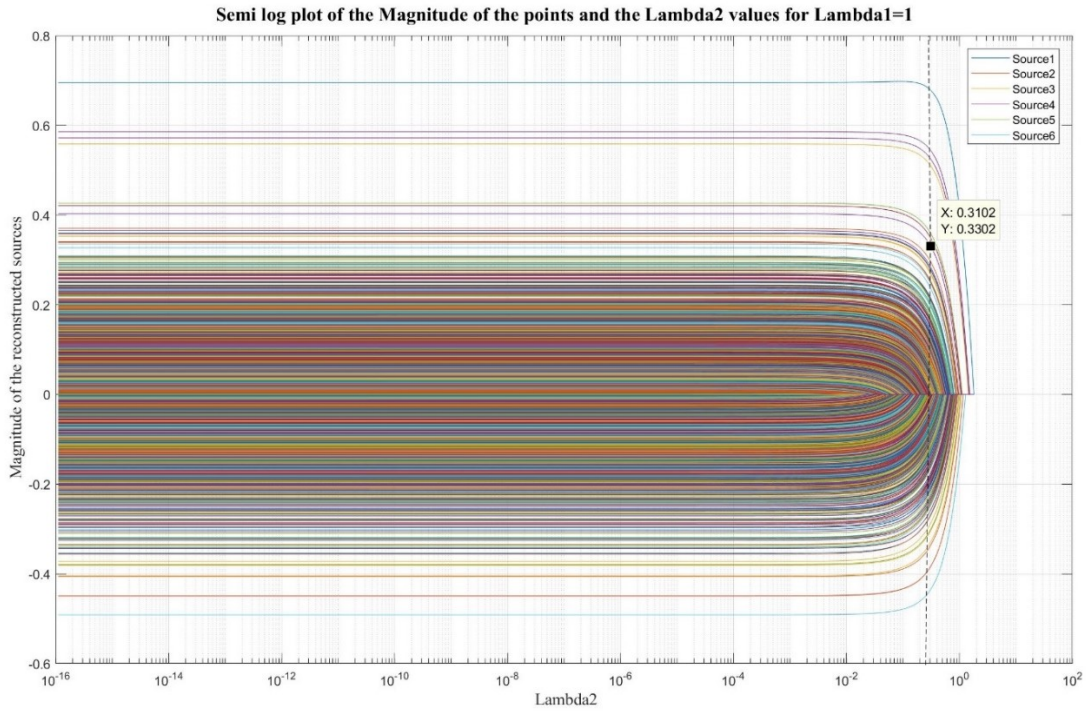

(b) Elastic net with λ_1=1

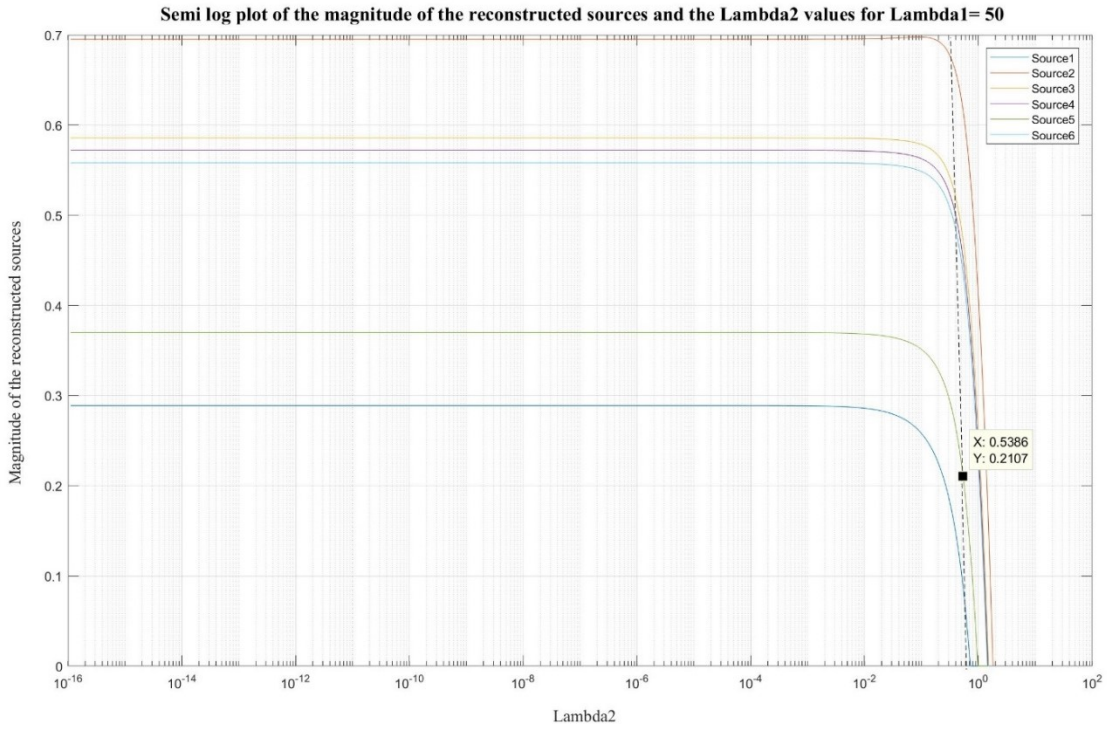

(c) Elastic net with λ_1=50

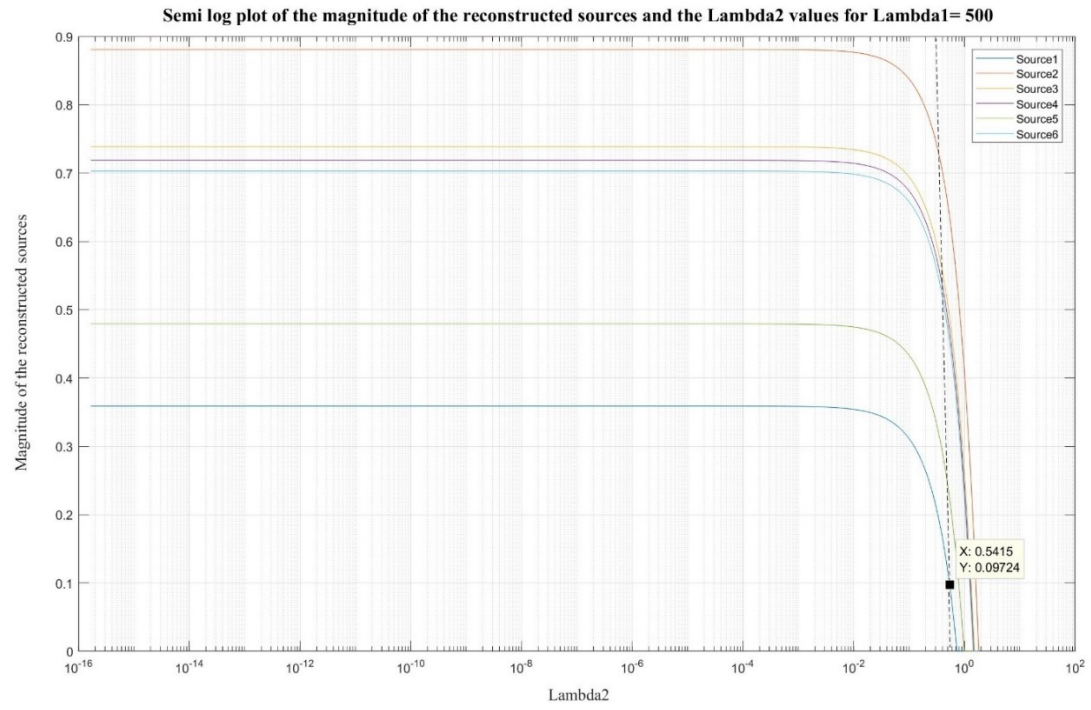

Figure 5.7 (a) Elastic net with λ_1=1e-2 (b) Elastic net with λ_1=1 (c) Elastic net with λ_1=50 (d) Elastic net with λ_1=500

A total of 2601 points are selected at random for performing the elastic net. For the purpose of illustrating the benefits of the elastic net over LASSO, all the six sources lie within these selected points. Figure 5.7 (a) and (b) show the variation in the magnitude with λ_2 for all the chosen points with the legend indicating the colour codes only for the reconstructed sources. The following figures show only the magnitudes of the six sources for the purpose of clarity.

It can be seen that Elastic Net is highly successful in reconstructing all the six sources with just four output nodes. When the λ_1 is very low as seen in Figure 5.7 (a), The effect of the LASSO penalty in the elastic net optimization equation is more than that of the ridge penalty. Hence, one of the six sources has a significantly higher magnitude than the rest of the sources. As the value of λ_1 is increased, the ridge penalty has more of an effect on the optimization than the LASSO. This reduces the significant difference in the magnitudes of the sources. The optimum value of λ_2 is chosen by selecting the minimum AIC for all λ_2 values for all the above cases. One such case is shown in Figure 5.8.

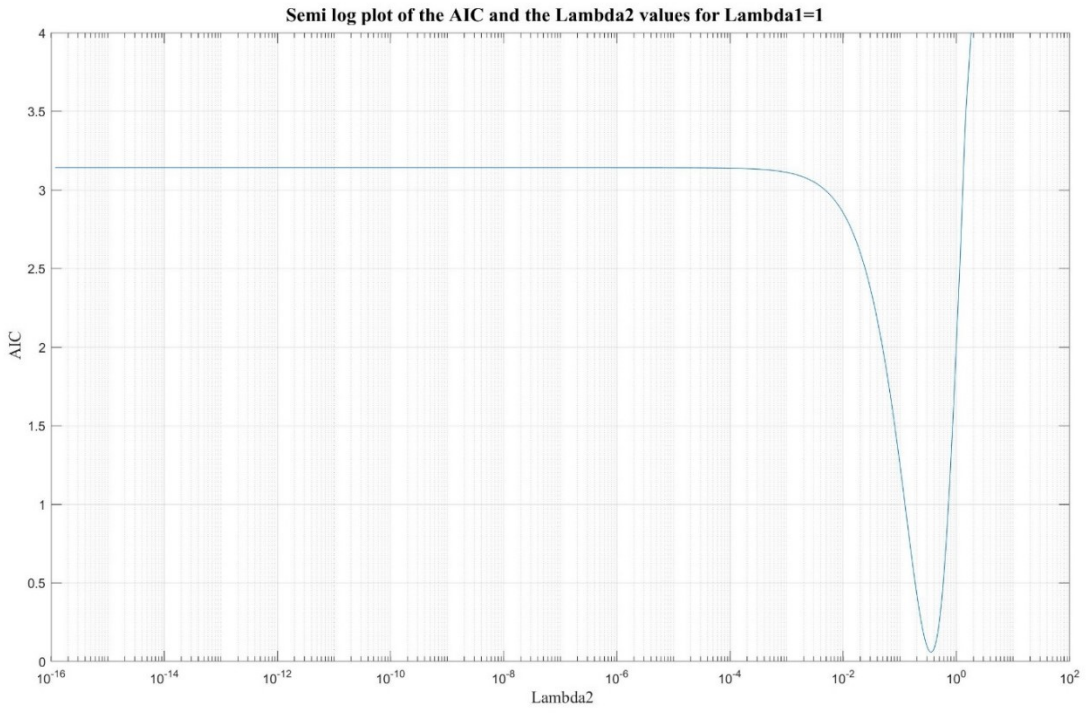

Figure 5.8 Choosing optimum lambda through the AIC criterion

The main limitation of using elastic net is the error in magnitude that is evident in Figure 5.7 (a) to (d). Hence, the elastic net is highly successful is recovering all the sources, it faces the problem of error in the recovery of magnitude and a few false peaks with magnitudes close to the original source as seen in Figure 5.7 (a) and (b).

5.4.2 Elastic Net for the second limitation

For the line source magnitude recovery, the elastic net is performed with optimum λ_2 and $\lambda_1 = 5$. Figure 5.9 depicts the difference in magnitude between the original and the reconstructed sources. Similar to the case of the first limitation, the elastic net is successful in recovering more sources than lasso but not all the 51. It also gives false peaks with magnitudes comparable to some of the reconstructed sources and exhibits lots of error in their magnitude. The same trend is seen with the increased value of λ_1.

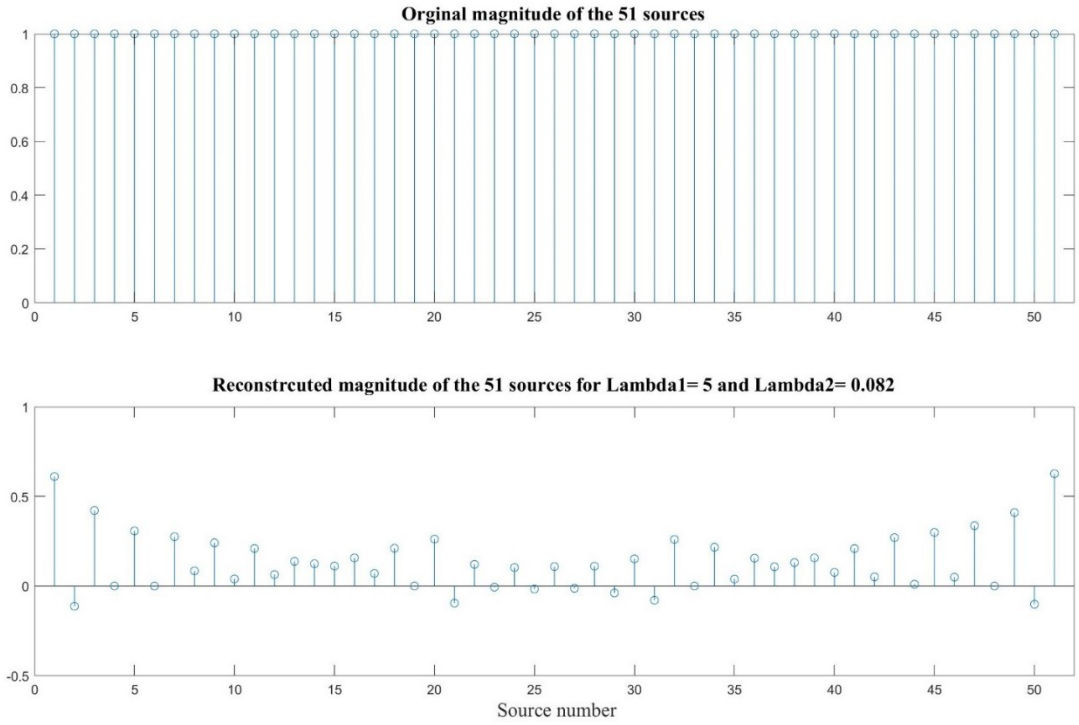

Figure 5.9 Magnitude comparison between original and reconstructed line of sources using Elastic net.

5.5 SUMMARY

The LASSO algorithm is very useful in the recovery of sources less than the number of output probes used. An alternative method of recovery with feature selection is analysed in Elastic net. Elastic net provides a trade-off between the dense solution of ridge regression and the sparse solution of LASSO regression. The recovery of the sources using the elastic net is a considerable improvement over the use of LASSO in doing the same. But the results do not provide the complete solution that is highly representative of the system. A subject of future research into the accurate recovery of the sources with different configuration could be other feature extraction methods. [25] gives a modified LASSO method called the group LASSO that considers the sparsity of a group of elements rather than individual vector elements. If the structure of the grouping of the sources is prior known, the group LASSO could provide the groups that contain the sources. More constraints on this solution might lead to complete solution. Higher order feature extraction methods in the realm of machine learning could also be used for the exact recovery of all the sources. The complete recovery of the different configuration of sources in two and three dimensions would constitute a major part of future research.

Chapter 6 APPLICATION OF TIME REVERSAL IN ANTENNA ARRAY FAILURE DIAGNOSIS

This chapter explores the array failure diagnosis application of time reversal. Antenna array failure diagnosis deals with the identification of faulty or inactive antenna elements in an antenna array. Time reversal is very useful in identifying the defective antenna elements. The fields from an antenna array of a specific geometry are recorded at different points. These values are reversed in time and reinjected back into the domain like the conventional time reversal process. The Section 6.1 applies the conventional time reversal to 2-D cavity that contains a 6 x 6 antenna array. Section 6.2 and 6.3 attempt the failure diagnosis for planar and non-planar arrays.

6.1 TWO-DIMENSIONAL ANTENNA ARRAY FAILURE DIAGNOSIS

In this section, array failure diagnosis is performed on a 6 x 6 antenna array with each antenna element considered as an impulse source. This antenna array is excited in a two-dimensional cavity surrounded with PEC boundary. To see the effectiveness of time reversal in failure diagnosis, three antenna elements are considered as failing elements as shown in Figure 6.1 (a). The time reversal operation is performed is performed with six output probes for 3000 iterations. Figure 6.1 (b) shows the reconstructed antenna array at the end of the final iteration. This clearly shows that time reversal can be applied to antenna array failure diagnosis.

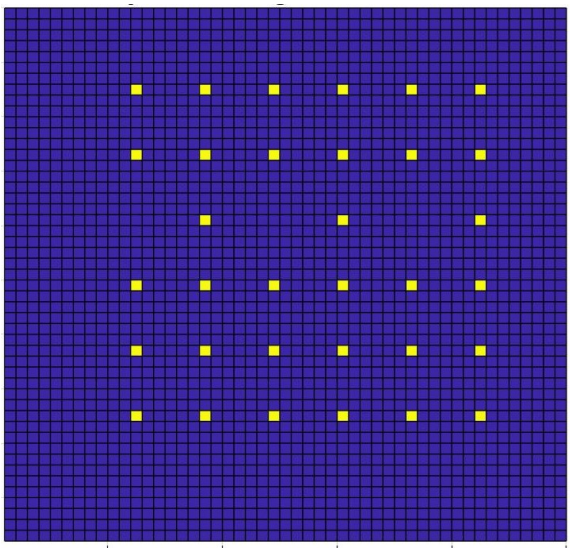

(a)

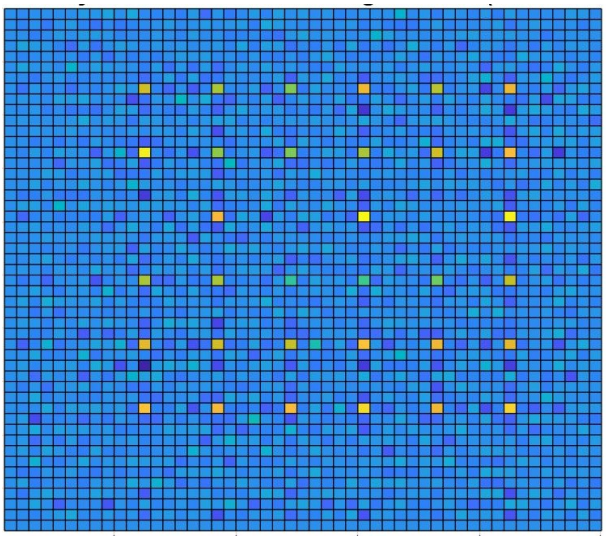

(b)

Figure 6.1 (a) 6 x 6 antenna array with three failing elements, (b) Reconstructed antenna array with no reconstructed peak at the failing element locations

6.2 THREE-DIMENSIONAL PLANAR ANTENNA ARRAY FAILURE DIAGNOSIS

In this section, the validity of the array failure diagnosis capability of time reversal is analysed for a 3-Dimensional cavity. The cavity that is used here is surrounded by a PEC to ensure reflection of the fields. The simulation is run for 5000 iterations. A 7 x 7 antenna array with impulse sources is excited in one z-plane. To illustrate the diagnosis capability 5 failure elements are considered as shown in Figure 6.3 (a). The same time reversal operation is performed, and the X-Y view of the reconstructed antenna array is shown in Figure 6.3(b). All the antenna elements except the failing antennas are reconstructed indicating the location of the failed antenna elements. The results can be extended to any geometry of planar antenna arrays.

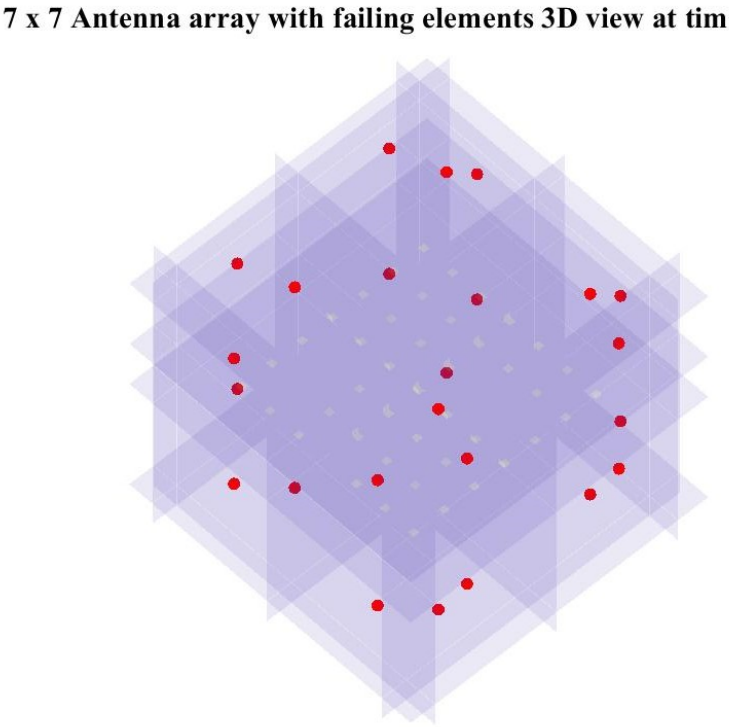

(a)

XY view of the 7 x 7 Antenna array with five failing elements at time step=1

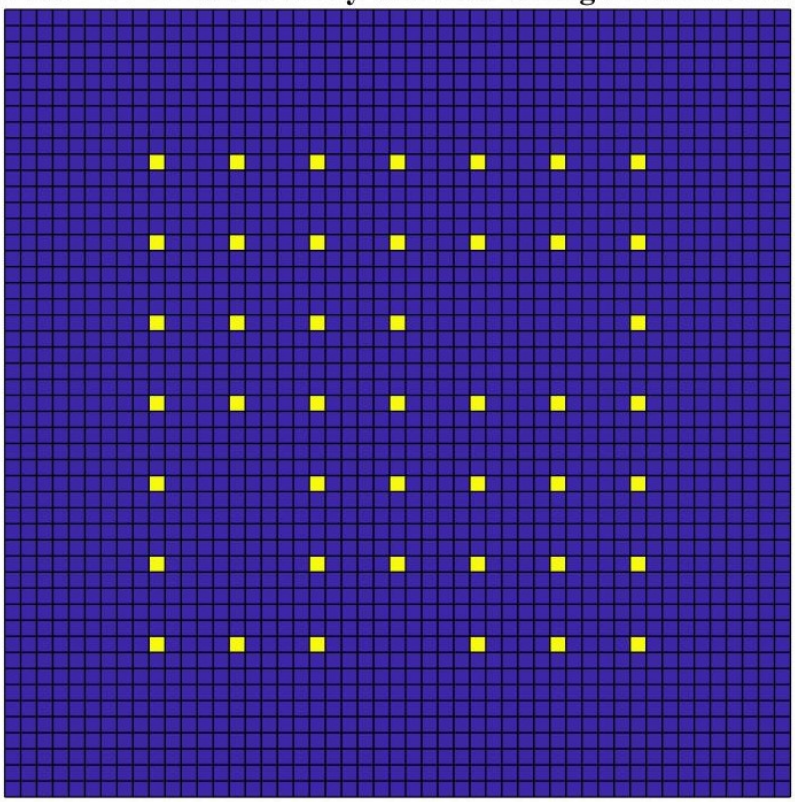

(a)

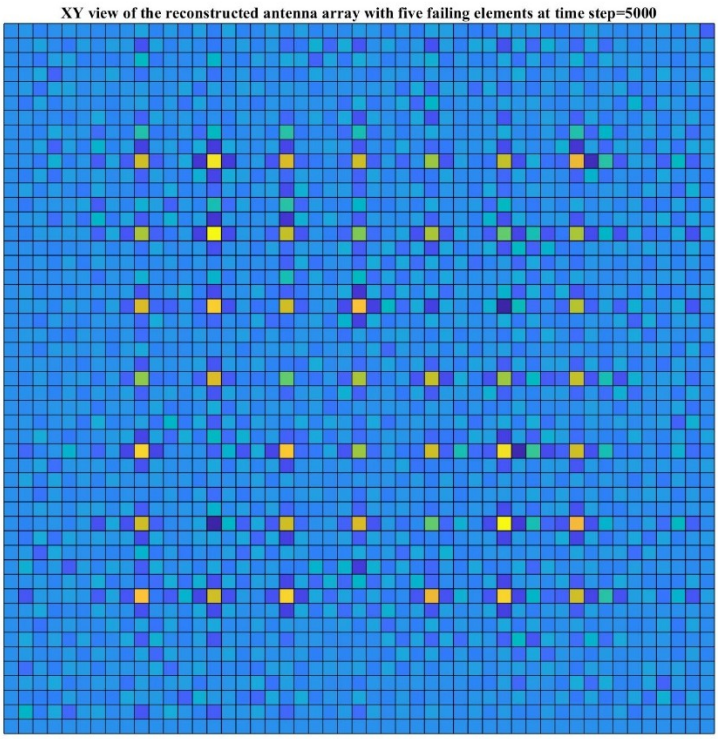

(b)

Figure 6.2 (a) 7 x 7 planar antenna array with five failing elements in three dimensions and the plane containing the array (b) X-Y view of the reconstructed antenna array with successful reconstruction of all the antenna elements except the failing elements.

6.3 ANTENNA ARRAY FAILURE DIAGNOSIS WITH ELEMENTS IN DIFFERENT PLANES

The failure diagnosis for non-planar antenna arrays is performed with three antenna array arrangements in three different z planes as shown in Figure 6.3. The first antenna array has one failing element, the second has three failing elements, and the third one has no failing elements. The time reversal algorithm is performed for 5000 iterations. Figure 6.4 shows the Z-planes containing the non-planar arrays perfectly reconstructed except for the failing antenna elements. Similar to the planar case, the non-planar failure diagnosis can be extended to different geometries.

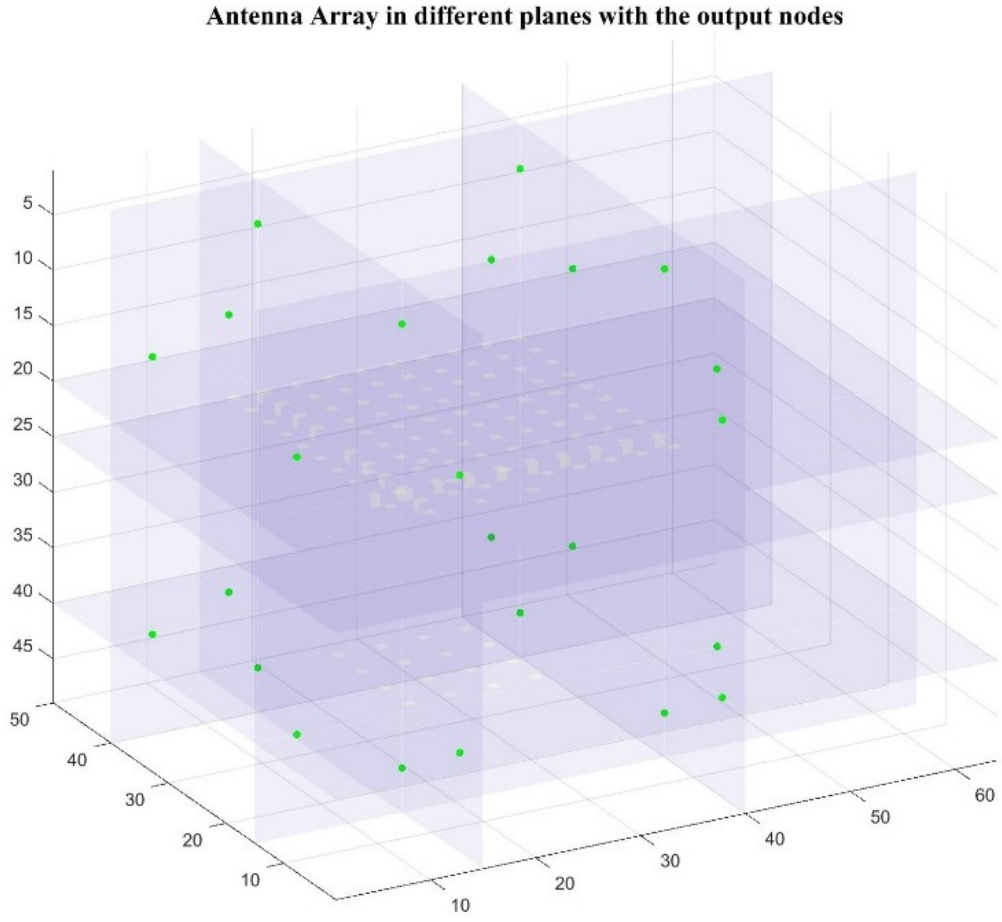

Figure 6.3 3D view of the three antenna arrays is different planes

Z-plane containing the first antenna array

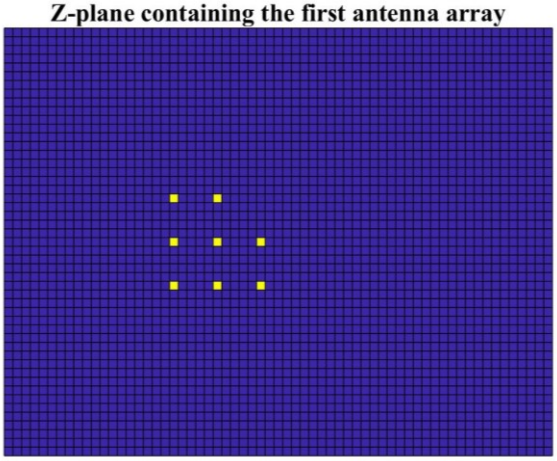

Z-plane containing the second antenna array

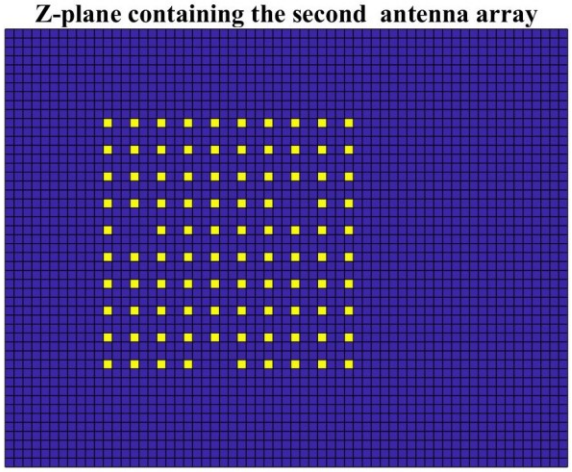

Z-plane containing the third antenna array

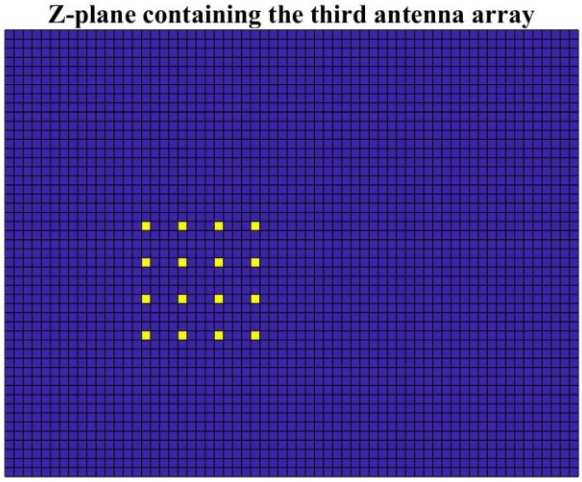

(a)

Z-Plane Containing the first reconstructed antenna array

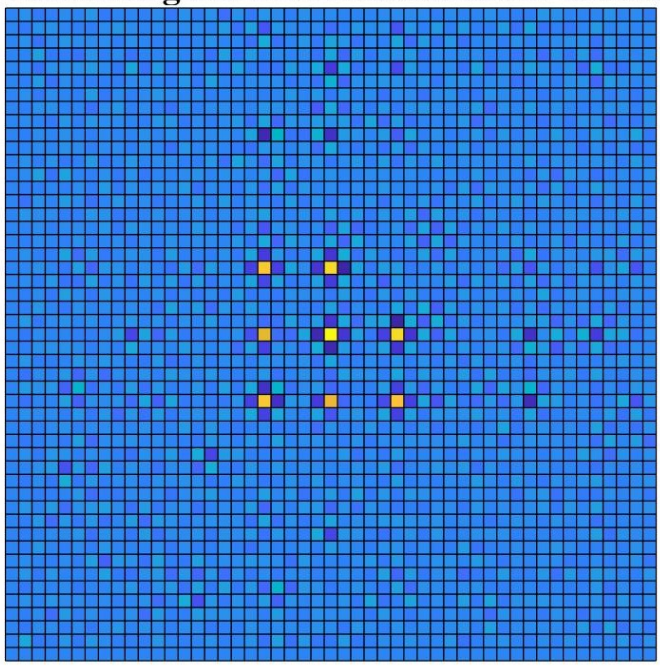

Z-Plane Containing the second reconstructed antenna array

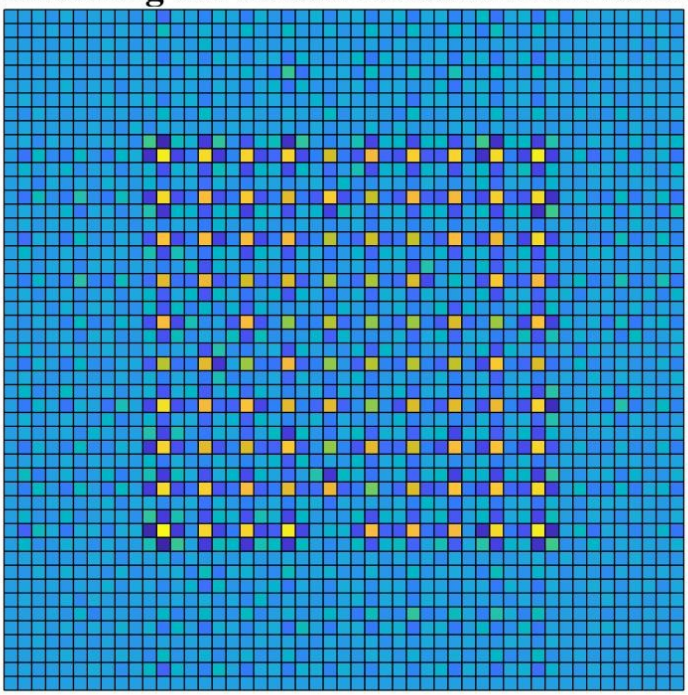

(b)

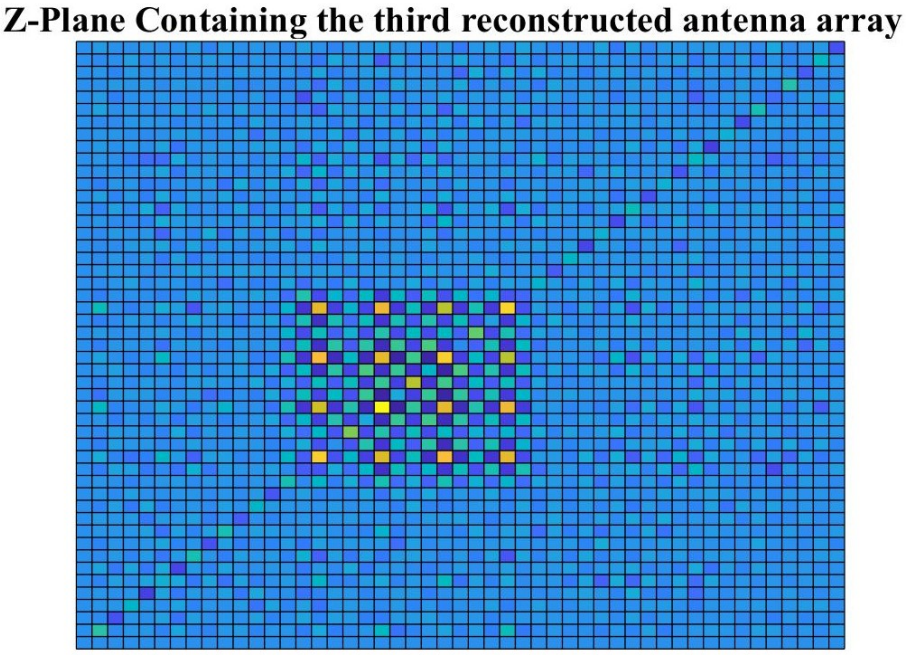

(b)

Figure 6.4 (a) 3D and the X-Y view of the three antenna arrays in different planes with failing elements. (b)X-Y views of the reconstructed non-planar antenna arrays with failing elements.

6.4 SUMMARY

This section focused on an application of time reversal in the failure diagnosis of antenna arrays. The failure diagnosis was explored in two and three dimensions and was applied to planar as well as non-planar antenna arrays. This proves that time reversal is very useful in the failure diagnosis of antenna arrays and robust for changing geometries and planes of antenna arrays. The practical realization of such an arrangement is an essential application for future research.

Chapter 7 CONCLUSION AND FUTURE WORK

7.1 CONCLUSION

This thesis has demonstrated the source reconstruction in two and three dimensions. Metrics used for the characterization of the focusing of the reconstructed sources were discussed. The metrics namely, the maximum energy of the source, space focusing gain and the signal to noise ratio in time were analysed for different configurations of the sources. These metrics were compared against the number of iterations of the FDTD algorithm, the number of output nodes used in the simulation and the distance of the output nodes from the sources. The maximum energy of the sources increases with increasing iterations and the number of output probes but remains unaffected with the change in position of the output nodes. The signal focusing gain shows a weak relation with the increase in iterations and output nodes while showing a sharp decrease and remaining at a constant level for the increase in the distance between the output node and the source. Similar to the SFG, the STRt shows a very little dependence on all the three categories. This leads to the conclusion that reliable reconstruction does not need many iterations, output nodes or closely located nodes.

The next chapter was the recovery of the magnitude of the sources. Existing methods based on LASSO were demonstrated, and its limitations were illustrated with the help of two examples. A different method was tested in the recovery of magnitude using the elastic net as the feature selection model. The elastic net proved to be a slight improvement over the LASSO in the recovery of all the sources but not the actual magnitude.

Antenna array failure diagnosis was realised using the conventional time reversal algorithm. It was tested in two and three dimensions for planar and non-planar antenna array. Time reversal proved to be very effective in the failure diagnosis of antenna elements.

7.2 FUTURE WORK

The metrics used in the performance analysis can be used to a domain surrounded with an absorbing boundary condition such as the perfectly matched layer. The results of this thesis can also be compared with the results when a device when an arbitrary permittivity is introduced in the domain.

More modified feature selection algorithms can be tested for the accuracy of the magnitude reconstruction. More research can be directed towards developing a problem specific constraint for the optimization problem in the magnitude recovery. The problem of the magnitude recovery could be treated as a high dimensional feature selection problem, and appropriate machine learning algorithms can be used to extract highly accurate magnitudes for the sources.

Practical application of time reversal could be realised with array failure diagnosis being the first step. Time reversal being an electromagnetic inverse problem can be applied for the calibration of phased antenna arrays. Time reversal can also be used to extract the properties of the medium after interaction. Another extension to the research in the thesis would be to apply magnitude recovery to find unwanted emissions in PCBs leading to an important EMC application.

REFERENCES

[1] K. S. Yee, "Numerical Solution of Initial Boundary Value Problem Involving Maxwell's Equations in Isotropic Media.," *IEEE Trans. Antennas and Propagation AP-14, vol 14,* pp. 302-307, 1966.

[2] A. Taflove, "Application of the finite-difference time-domain method to sinusoidal steady-state electromagnetic-penetration problems," *IEEE Transactions on Electromagnetic Compatibility, Vol EMC-22,* pp. 191-202, 1980.

[3] S. Gedney, "Introduction to the finite difference time domain (fdtd) method for electromagnetics," *Synthesis lectures on computational electromagnetics,* vol. 6, pp. 1-250, 2011.

[4] A. Taflove and S. C. Hagness, *Computational Electrodynamics: The Finite Difference Time Domain Method*, Norwood, MA: Artech House, 1995.

[5] A. Taflove, *Advances in Computational Electrodynamics: The Finite Difference Time Domain Method*, Norwood, MA: Artech House, 1998.

[6] D. M. Sullivan, "A frequency-dependent FDTD method for biological applications," *IEEE Transactions on Microwave Theory and Techniques,* vol. 40, no. 3, pp. 532-539, 1992.

[7] L. Sevgi and F. Bilotti, "Metamaterials: Definitions, properties, applications, and FDTD-based modeling and simulation," *International Journal of RF and Microwave Computer-Aided Engineering,* vol. 22, no. 4, pp. 422-438, 2012.

[8] F. Torres and B. Jecko, "Complete FDTD analysis of microwave heating processes in frequency-dependent and temperature-dependent media," *IEEE Transactions on Microwave Theory and Techniques,* vol. 45, no. 1, pp. 108-117, 1997.

[9] M. Fink, D Cassereau,A Derode, C Prada,P Roux, M Tanter,J-L Thomas and F Wu, "Time Reversed Acoustics," *Reports on Progress in physics,* vol. 63, number 12, pp 1933, 2000.

[10] G. Lerosey, J de Rosny, A Tourin, A Derode, G Montaldo and M Fink "Time Reversal of Electromagnetic Waves," *Physical Review Letters,* vol. 92, no. 19, pp.193904, 2004.

[11] G. Lerosey, J de Rosny, A Tourin, A Derode, G Montaldo and M Fink, "Time Reversal of Electromagnetic Waves and Telecommunication,", vol 40, no. 6, pp. 1-10, 2005.

[12] W. J. Hoefer, "Computational Time Reversal—A Frontier in Electromagnetic," *IEEE Transactions on Microwave Theory and Techniques,* vol. 63, no. 1, pp. 3-10, 2015.

[13] M. Forest and W. J. Hoefer, "TLM synthesis of microwave structures using time reversal," *Microwave Symposium Digest,* Albuquerque, NM, USA, pp. 779-782, 1992.

[14] P So, W. J. Hoefer, R. Sorrentino, "Numerical microwave synthesis by inversion of the TLM process," in *1991 21st European Microwave Conference*, Stuttgart, Germany, 1991.

[15] L. Roselli, P Mezzanotte and R. Sorrentino, "Time reversal in finite differnce time domain method," *IEEE Microwave and Guided Wave Letters,* vol. 3, pp. 402-404, 1993.

[16] P. Kosmas and C. M. Rappaport, "Time reversal with the FDTD method for microwave breast cancer detection.," *IEEE Transactions on Microwave Theory and Techniques,* vol. 53, no. 7, pp. 2317-2323, 2005.

[17] Z. Chen, W. J. R. Hoefer and W. Fan, "Source Reconstruction From Wideband and Band-Limited Responses by FDTD Time Reversal and Regularized Least Squares," *IEEE Transactions on Microwave Theory and Techniques,* vol. 65, no. 12, pp. 4785-4793, 2017.

[18] W. Fan and Z. Chen, "A condition for multiple source reconstructions with the time-reversal methods," in *2016 IEEE MTT-S International Microwave Symposium (IMS)*, San Fransico, CA, 2016, pp1-4.

[19] K. Friedrichs,H. Lewy and R. Courant, "Über die partiellen Differenzengleichungen der mathematischen Physik," *Mathematische annalen,* vol. 100, pp. 32-74, 1928.

[20] A. D. Kim,G. Papanicolau, A. J. Paulraj and C. Oestges, "Characterization of space-time focusing in time-reversed random fields," *IEEE Transactions on Antennas and Propagation,* vol. 53, no. 1, pp. 283-293, 2005.

[21] M. F. Wong, J. Wiart and Y. Ziade, "Reverberation chamber and Indoor measurements for time reversal application," *In Proc. IEEE Antennas and Propagation Society International Symposium,* pp. 1-4, 2008.

[22] D. Donoho, "For most large underdetermined systems of equations, the minimal ℓ1-norm near-solution approximates the sparsest near-solution," *Communications on Pure and Applied Mathematics,* pp. 907 - 934, 2006.

[23] H. Akaike, "Information Theory and an Extension of the Maximum Likelihood Principle," in *Proceedings of the 2nd International Symposium on Information Theory*, Budapest, 1973.

[24] G. Schwarz, "Estimating the Dimension of a Model," *Ann. Statist,* vol. 6, no. 2, pp. 461--464, 1978.

[25] R. Tibshirani, T Hastie and J Friedman, *The Elements of Statistical Learning*, New York, 2001.

[26] K. Sjöstrand, "Matlab implementation of LASSO, LARS, the elastic net and SPCA," *Informatics and Mathematical Modelling, Technical University of Denmark, {DTU},* 2005.

[27] A. E Hoerl and R W Kennard "Ridge Regression: Biased Estimation for Nonorthogonal Problems," *Technometrics,* vol. 12, no. 1, pp. 55-67, 1970.

[28] H. Zou and T. Hastie, "Regularization and Variable Selection via the Elastic Net," *Journal of the Royal Statistical Society ,* Vol 67, no. 2, pp. 301-320, 2005.

[29] M. Rubinstein, F. Rachidi, M. Paolone, *Time Reversal: A Different Perspective: Application to EMC and Power Systems,* Wiley, 2017.

[30] T. Hastie, R. Tibshirani and H. Zou, "On the “degrees of freedom” of the lasso," *Ann. Statist,* vol. 35, no. 5, pp. 2173-2192, 2007.